Effects of natural surfactants on the spatial variability of surface water temperature under intermittent light winds on Lake Geneva

Mehrshad Foroughan, Ulrich Lemmin, David Andrew Barry

Ecological Engineering Laboratory (ECOL), Environmental Engineering Institute (IIE), Faculty of Architecture, Civil and Environmental Engineering (ENAC), Ecole Polytechnique Fédérale de Lausanne (EPFL), Lausanne, Switzerland

ABSTRACT

The spatial variability of Lake Surface Water Temperature (LSWT) between smooth and rough surface areas and its potential association with the natural surfactant distribution in the surface microlayer were investigated for the first time in a lake. In spring 2019, two different field campaigns were carried out in Lake Geneva to measure: (i) the enrichment factor of Fluorescent Dissolved Organic Matter (FDOM) as a proxy for biogenic surfactants, and (ii) LSWT and near-surface water temperature profiles while simultaneously monitoring water surface roughness in both cases. Results indicate that, under intense incoming short-wave radiation and intermittent light wind conditions, the Atmospheric Boundary Layer (ABL) was stable and the accumulation of heat due to short-wave radiation in near-surface waters was greater than heat losses by surface cooling, thus creating a diurnal warm layer with strong thermal stratification in the water near-surface layer. A threshold wind speed of 1.5 m s^{-1} was determined as a transition between different dynamic regimes. For winds just above 1.5 m s^{-1}, the lake surface became patchy, and smooth surface areas (slicks) were more enriched with FDOM than rough areas (non-slick) covered with Gravity-Capillary Waves (GCW). Sharp thermal boundaries appeared between smooth and rough areas. LSWT in smooth slicks was found to be more than 1.5°C warmer than in rough non-slick areas, which differs from previous observations in oceans that reported a slight temperature reduction inside slicks. Upon the formation of GCW in non-slick areas, the near-surface stratification was destroyed and the surface temperature was reduced. Furthermore, winds above 1.5 m s^{-1} continuously fragmented slicks causing a rapid spatial redistribution of LSWT patterns mainly aligned with the wind. For wind speeds below 1.5 m s^{-1} the surface was smooth, no well-developed GCW were observed, LSWT differences were small, and strong near-surface stratification was established. These results contribute to the understanding and the quantification of air-water exchange processes, which are presently lacking for stable Atmospheric Boundary Layer conditions in lakes.

Corresponding author: mehrshad.foroughan@epfl.ch

Key words: Surface water temperature, surfactant, diurnal warm layer, slicks, low wind, gravity-capillary waves.

Citation: Foroughan M, Lemmin U, Barry DA. Effects of natural surfactants on the spatial variability of surface water temperature under intermittent light winds on Lake Geneva. *J. Limnol. 2022;81:2048.*

Edited by: Marco Toffolon, *Department of Civil, Environmental and Mechanical Engineering, University of Trento, Italy.*

Received: 12 July 2021.
Accepted: 31 May 2022.

J. Limnol., 2022; 81:2048
DOI: 10.4081/jlimnol.2022.2048

INTRODUCTION

In lakes and oceans, surface water temperature is a key parameter controlling the air-water exchange of heat, momentum, and mass. Surface water temperature and these exchanges are not only influenced by turbulence and waves mainly forced by wind (*e.g.*, Garbe *et al.*, 2004; MacIntyre *et al.*, 2021b), but also by surface surfactant layers (*e.g.*, Frew *et al.*, 2004; Pereira *et al.*, 2018). These processes generally show strong spatial variations, manifested by nonuniform surface water temperature patterns, which can affect flux estimates at the air-water interface (Hughes *et al.*, 2012; Rahaghi *et al.*, 2019a), and therefore should be taken into account when addressing climate warming scenarios (Calamita *et al.*, 2021). Although wind-induced surface water temperature dynamics have been investigated (Kawai and Wada, 2007; Zappa *et al.*, 2019), the effect of surfactants on surface water temperature is less documented in oceanic studies (Marmorino and Smith, 2006), and apparently has never been investigated in lakes.

Surfactants are surface-active substances that can originate from phytoplankton metabolic byproducts (Žutić *et al.*, 1981), marine bacterial activities (Kurata *et al.*, 2016), zooplankton grazing (Kujawinski *et al.*, 2002) and, in par-

ticular for lakes, from terrestrial sources (Hunter and Liss, 1981) introduced by rivers when the riverine inflow reaches the near-surface layer (Masse and Murthy, 1990; Soulignac *et al.*, 2021). The accumulation of natural surfactants in the water surface microlayer attenuates small waves, thus creating smooth surface areas referred to as natural slicks (Liss and Duce, 1997; Gade *et al.*, 2006). Slicks are significantly more enriched with particles and dissolved material compared to surrounding non-slick (rough) surfaces (Garabetian *et al.*, 1993; Wurl *et al.*, 2016). Previous slick *vs.* non-slick area comparisons in oceans reported higher concentrations of surfactant-associated bacteria (Kurata *et al.*, 2016), larval fish and microplastics (Gove *et al.*, 2019) inside the smooth surface layers. Chlorophyll has also been used as a surfactant proxy in estimates of surfactant activity (Tsai and Liu, 2003) and its spatial distribution (De Santi *et al.*, 2019). Under light to moderate wind conditions (<6 m s^{-1}, McKinney *et al.*, 2012), smooth surfactant-rich slicks and rough/rippled areas with low surfactant concentrations form distinct patches (Fig. 1) and are distributed on most water bodies (Romano, 1996; Engel *et al.*, 2017).

When surfactants exceed a critical concentration, they alter the surface boundary conditions by introducing non-zero dilational viscoelasticity to the uppermost layer of the water (Frew, 1997). Dilational viscoelasticity links stress and strain at the air-water interface in response to a small expansion and compression of a surface area (Watson *et al.*, 1997). This affects near-surface hydrodynamics by thickening the water-side viscous sublayer (Tsai, 1996) and dampening Gravity Capillary Waves (GCW) (Alpers and Hühnerfuss, 1989), which can, in turn, modulate air-water exchanges. Since slick surfaces are smooth compared to those of rough non-slick areas, they can be

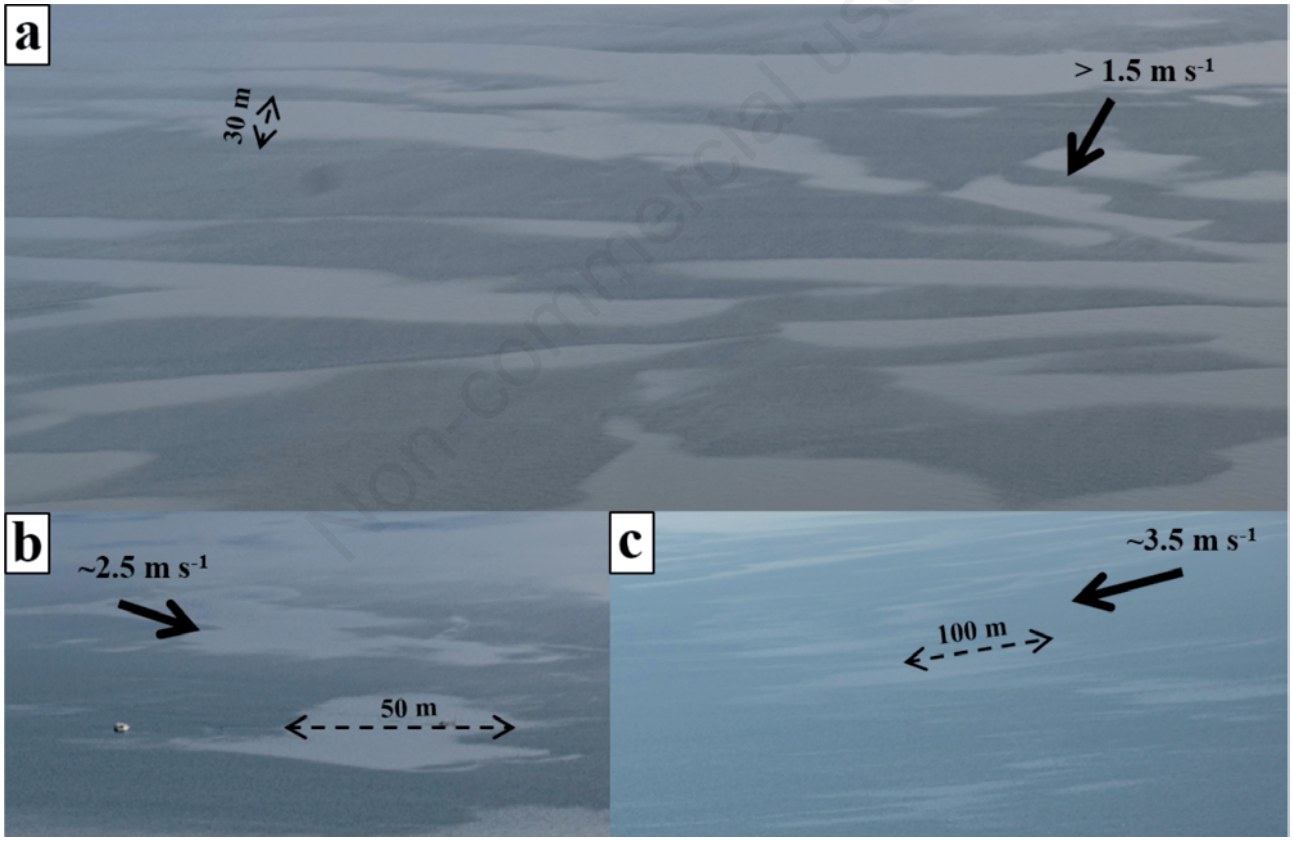

Fig. 1. a) Aerial view of slick and non-slick areas on the surface of Lake Geneva (for location, see Fig. 2) recorded in April 2021 by a remotely-operated camera system (RGB) installed 195 m above the lake surface water and ~440 m away from the shore. This is a typical example of surface patterns frequently observed anywhere on the lake under stable atmospheric boundary layer conditions and low wind (solid-line arrows indicate direction and speed). Smooth slick and rough/rippled non-slick areas are easily distinguishable due to differences in the surface reflection; smooth slicks are more visible because of their increased specular light reflection. b) and c) Slick distribution under higher wind speed conditions (taken in March 2021). With increasing wind speed, slick areas decrease and eventually transform into streaks parallel to the wind. Dashed-line double arrows give length scales. Analysis of surface water samples during those two days showed higher organic matter enrichment inside slicks (data not shown).

observed visually (Fig. 1), or by Synthetic Aperture Radar (SAR) inside convergent zones produced by internal waves (Alpers, 1985; Whitney *et al.*, 2021), Langmuir circulation (Marmorino *et al.*, 2007), mesoscale and submesoscale eddies (Schuler and Lee, 2006; Karimova, 2012; McKinney *et al.*, 2012), and coastal upwelling and filaments (Dabuleviciene *et al.*, 2018; Hamze-Ziabari *et al.*, 2022). These underlying hydrodynamic processes, along with the direct effect of wind, contribute to the formation, distribution, and disintegration of slick patterns. Such dynamics, however, have not been documented in lakes

The effect of biogenic surfactants on near-surface hydrodynamics can also result in surface water temperature heterogeneity. In a laboratory experiment, Jarvis (1962) observed changes in surface temperature by adding artificial surfactants to the water. The temperature shift was either caused by the barrier effect of the surfactant monolayer, preventing evaporation, or by the suppression of near-surface turbulence (Bower and Saylor, 2011). The latter effect is predominant in natural environments, and biogenic surfactants typically do not show barrier-like behavior (Liss, 1983). Frew *et al.* (2004) and Marmorino and Smith (2006) reported that slicks are slightly colder than the surrounding non-slick water in the ocean under unstable ABL conditions and surface cooling. Under strong solar radiation and low wind conditions, a thin warm near-surface layer develops in the water when solar heating exceeds heat loss from the water surface, and as a result, a Diurnal Warm Layer (DWL) (Price *et al.*, 1986) or a diurnal thermocline (Imberger, 1985) is formed. Past slick field studies compared the surface water temperature to the bulk temperature (assumed constant), measured well below the water surface (Marmorino and Smith, 2006). However, DWL formation and temperature gradients in the near-surface layer were not considered in their analyses.

Air-water exchange dynamics are different under stable and unstable Atmospheric Boundary layer (ABL) (Kara *et al.*, 2005; Mahrt and Hristov, 2017). Although near surface dynamics under stable ABL conditions have been studied in lakes during events (*e.g.*, Yusup and Liu, 2016; Rahaghi *et al.*, 2019b), their potential differences in slick and non-slick areas under stable ABL and light wind conditions during DWL formation have not yet been reported. However, these differences can strongly affect air-water exchange. In Lake Geneva, it was shown that winds are light (<4 m s^{-1}) 80 - 90% of the time during the stratification period (May to October; Lemmin and D'Adamo, 1996). Stable ABL conditions have been observed to last for several months in spring and early summer (Rahaghi *et al.*, 2019b; Lemmin, 2020), thus indicating that stable ABL, low wind conditions are important in the annual air-water exchange cycle.

The present study, carried out in Lake Geneva, will therefore, for the first time in a lake, explore the effect of light wind and surfactants on the spatial variability of Lake Surface Water Temperature (LSWT) under stable ABL conditions. In a novel approach, high-resolution near-surface water temperature profiles were combined with surface temperature measurements and real-time monitoring of water surface roughness. The following questions are addressed:

Can the ability of surfactants to form slicks and affect wind wave development influence the near-surface thermal structure? If so, under what conditions?

What is the potential relationship between LSWT variability and natural surfactants in the surface microlayer as a function of wind speed? Is there a wind speed threshold?

What is the LSWT difference between smooth slicks and rough surface areas during DWL formation? What causes this difference?

MATERIALS AND METHODS

Study site

In 2019, two field measurement campaigns were performed on Lake Geneva (Local name: *Lac Léman*), a warm oligomictic perialpine lake situated between Switzerland and France at a mean altitude of 372 m. It is Western Europe's largest lake with a length of 70 km, a maximum width of 14 km, a surface area of 582 km^2, a volume of 89 km^3, and a maximum depth of 309 m (Fig. 2a). The surrounding mountainous topography strongly affects the wind field and, as a result, the shear stress distribution over the lake (Razmi *et al.*, 2017; Rahaghi *et al.*, 2019a). In addition to the two strong dominant winds called *Bise* and *Vent*, fishermen have identified over 20 local wind fields that often have low wind speeds and only act on parts of the lake surface.

Measurement platforms for physical parameters

Measurements were taken from a mobile, two-platform system consisting of: (i) a 7-m long autonomous catamaran (called ZiviCat), and (ii) a 9-m^3 balloon (called BLIMP) carrying an imaging package beneath it (Fig. 3). The ZiviCat is equipped with a set of *in situ* near-surface (down to 1.5 m) water temperature sensors (RBRsolo, accuracy: 0.002°C, 1 Hz), a weather station (Airmar 200WX IPX7) installed at 3-m height, with motion-corrected outputs for wind speed, wind direction, and air temperature (0.66 Hz), a relative humidity sensor at 2.8-m height (1 Hz), and an RGB Raspberry Pi camera at 1.2-m height that captures images of the lake surface in front of the ZiviCat for a qualitative measure of surface roughness. The sensor spar is located well forward of the catamaran to avoid hull disturbances. The ZiviCat also has positioning (RTK-GPS), stability (IMU), data recording, and communication systems, which allow for real-time data

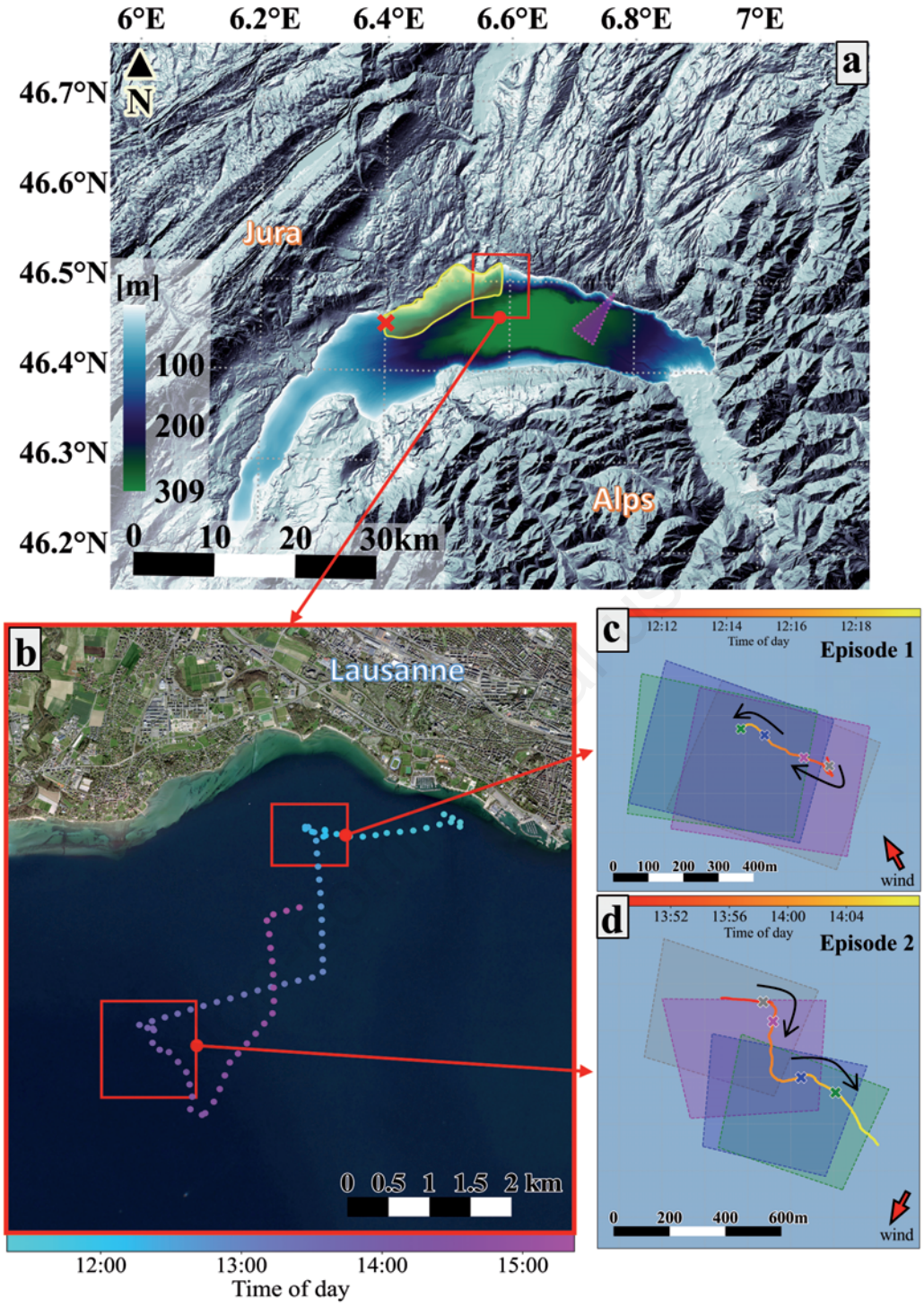

Fig. 2. a) Location and bathymetry of Lake Geneva, and the topography of the mountain ranges surrounding the lake, *i.e.*, the Alps to the southeast and the Jura to the northwest. The magenta triangle shows the approximate field of view of the camera system in Fig. 1. The yellowish region along the lake's northern shore represents the area where water sampling campaigns were conducted. The red square delimits the study area. The red X marks the meteo station Buchillon. b) Zoom of red square in (a) showing the catamaran ZiviCat track in the northern part of Lake Geneva near Lausanne on 18 April 2019. The red squares indicate the sites of the two episodes. c) and d) Zooms of the study sites in b). The four colored rectangles illustrate the geo-referenced spatial extent of the thermal snapshots in Figs. 6 and 7. The gray, magenta, blue, and green areas and the symbols along the tracks correspond, respectively, to panels c, d, e, and f of those figures. In all panels, colorbars indicate the time along the catamaran tracks. Black arrows in c) and d) show the direction of the catamaran movement. Red arrows give the mean wind direction during the Episodes.

control, correction and analysis on the accompanying boat (Barry *et al.*, 2019).

The BLIMP is tethered to a winch on the accompanying boat (Fig. 3). For the measurement campaign, the balloon was positioned approximately 500 m above the lake surface, which resulted in a surface spatial resolution of 0.8 m and an image width of about 400 m. The imaging package includes a FLIR Tau 2 Long-wave Infrared (IR) camera (7.5-13.5 µm spectral range, 640 × 512 pixel resolution, 14-bit digital output) and an RGB Raspberry Pi camera for visual inspection, as well as equipment for positioning (GPS), orientation, tilt angles, and communication with the boat (Liardon and Barry, 2017). BLIMP images were corrected for nonuniformity, *i.e.*, spatial noise caused by different detector responses in the focal plane array (the core of an uncooled IR sensor), following a two-point calibrated-based method (Rahaghi *et al.,* 2019c), as well as temporal drift. The pretreated images were then radiometrically calibrated using the temperature measurements taken at 5-cm depth by the ZiviCat. Despite the correction, some residual errors can remain in the thermal images' upper left and lower right corners (Figs. 6 and 7; Rahaghi *et al.,* 2019c). Therefore, those regions should be interpreted with caution. The uncertainty associated with emissivity variation due to surface roughness modulations is negligible with a low bias, since the incident angle (<10°) for image acquisition of the BLIMP package is low (Cheng *et al.*, 2019; Zappa *et al.*, 2019). The mobile ZiviCat-BLIMP system allowed following water mass parcels in real time as they trans-

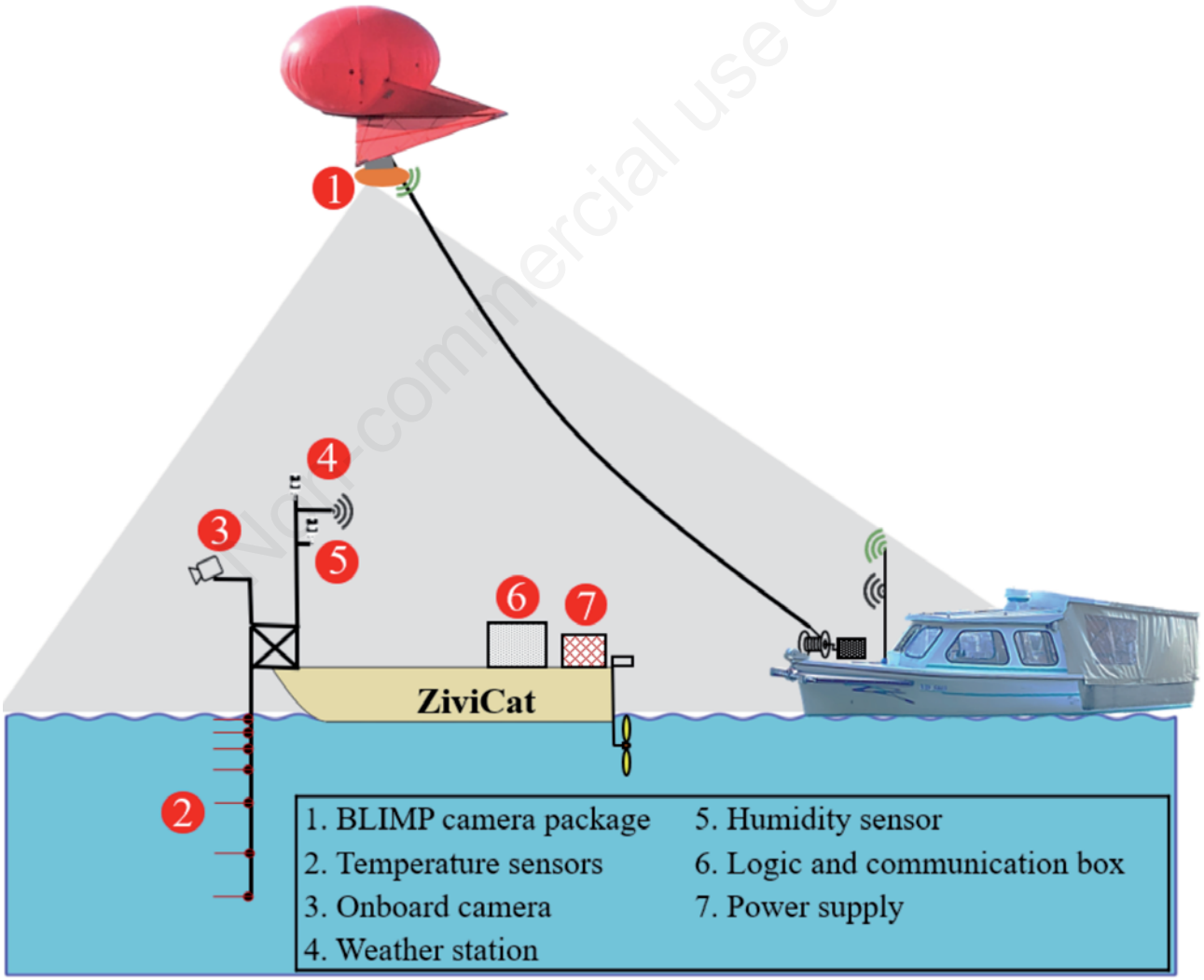

Fig. 3. Schematic of the mobile two-platform measurement system consisting of the 9-m^3 balloon called BLIMP and the remotely operated catamaran called ZiviCat. Data collected by the BLIMP and ZiviCat were transmitted to the accompanying boat, the *Elodea*, where they could be visualized in real time. The legend identifies the different sensors on the BLIMP and the ZiviCat.

formed from smooth slicks areas to rough/rippled areas and *vice versa*.

Field Campaign 1:
Surface water sampling and surfactant analysis

In situ measurement of the viscoelastic modulus provides the most direct evidence for determining the slick's ability to modulate wind-wave development and air-water exchanges (Watson *et al.*, 1997). However, in previous ocean studies, slick and non-slick regions were usually classified by measuring a proxy for surfactant concentration in water samples. Simultaneous water sampling during the ZiviCat/BLIMP measurements was not possible due to the different strategies required for each campaign. Therefore, in order to establish a reliable database on surfactant dynamics, separate water sampling field missions were conducted from 10:00 to 14:00 (local time) on 22 January, 15 February, 21 March, and 17 July 2019 in an area off the lake's northern shore (Fig. 2a). A meteo station (Buchillon mast; red X in Fig. 2a) near the sampling sites recorded no clouds and the following wind speeds on these four days: 1.53±0.45, 1.3±0.35, 3±0.55, 1.8±0.35 m s^{-1}, respectively. The maximum solar radiation increased from 480 W m^{-2} in January to 980 W m^{-2} in July, while atmospheric stability changed from unstable to stable. Surface water samples were taken from visually-identified areas of smooth and surrounding rippled water. Such surface roughness patterns are typically generated in Lake Geneva under low wind conditions (*e.g.*, Fig. 1), and can form anywhere on the lake. The glass-plate method was used to collect the uppermost 20-150 µm of the surface (Cunliffe *et al.*, 2013) as well as hand-dipping to sample bulk water (20 cm below the surface) following standard procedures (Cunliffe and Wurl, 2014). The samples were brought back to the laboratory for further analysis, usually performed on the same day.

The enrichment of Fluorescent Dissolved Organic Matter (FDOM) was chosen as a proxy for biogenic surfactants (Frew *et al.*, 2002; Salter, 2010). Samples were analyzed in a Fluorescence Spectrometer (Perkin Elmer) that provided an Excitation Emission Matrix (EEM) for each sample (Fig. 4a). The EEM was constructed by as-

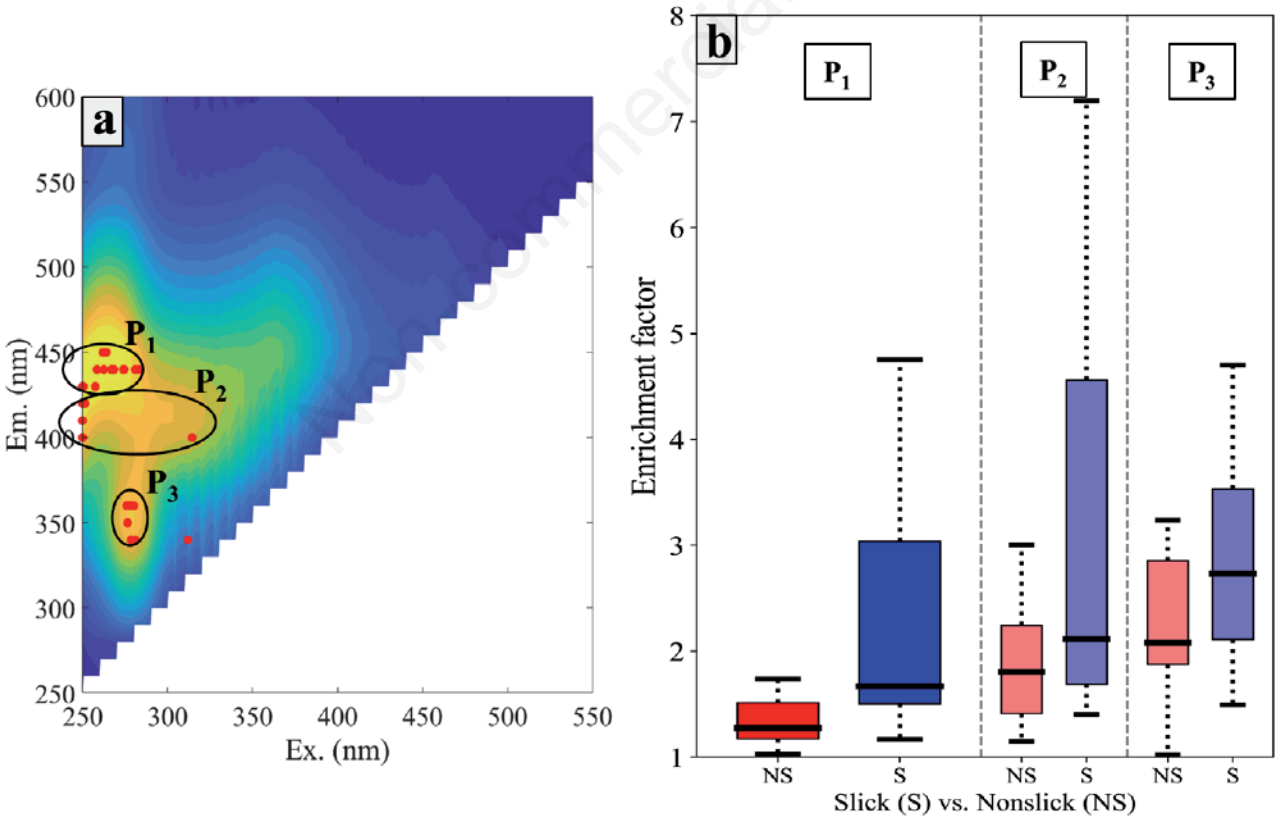

Fig. 4. a) The integration of the three components (peaks) P1, P2, and P3 identified with PARAFAC analysis. On the plot, the dominant peaks in each sample (obtained prior to PARAFAC analysis) are displayed as red dots, with black ellipses grouping them into three categories based on Murphy *et al.* (2008). b) Box plot of the FDOM enrichment factor for components P1, P2, and P3 observed in the EEM matrix. Red/blue boxes show the interquartile range (25-75%) for Non-slick (NS) and Slick (S) areas, respectively, and tails (dashed lines) indicate the 1-99 percentile range. Heavy black lines in the boxes are the medians.

sembling emission spectra (250-600 nm) within a range of excitation wavelengths (250-550 nm). Since different organic materials fluoresce differently, one or several peaks (components) can appear in the EEM. To determine the location of peaks (emission/excitation wavelength) and the contribution of each sample to that peak, parallel factor analysis was applied (PARAFAC, see Stedmon and Bro, 2008) to the EEMs of all samples (Fig. 4b).

Following Frew *et al.* (2002), the component close to 450 nm (emission) was selected to compute the Enrichment Factor (EF) for each sample set (surface and bulk). However, other peaks (components) appeared in the EEMs. The EF is calculated as the ratio of surface fluorescence intensity to the bulk values, which is proportional to the EF of surfactant activity (Salter, 2010). A permutation test was performed to compare the samples from slick and non-slick areas (Gove *et al.*, 2019) in order to estimate the probability that the mean enrichment factor of FDOM inside a slick (EF_i) is larger than that in the ambient water (EF_o), i.e., $P(EF_i > EF_o)$. To compute this probability, we first permutated the labels (slick or non-slick) randomly for all samples, then recalculated the test statistic ($EF_i - EF_o$). After sufficient permutations (*e.g.*, 10,000), an approximate distribution of the test statistic can be obtained. The p-value was then calculated, which is the probability of getting a larger difference of mean EFs than the difference in the original data.

Field Campaign 2: LSWT patterns and near-surface stratification

The ZiviCat/BLIMP measurements were made on 18 April 2019 in the daytime under high solar radiation (maximum above 700 W m^{-2}) and low-wind conditions (<2.5 m s^{-1}) during the early stages of the seasonal stratification period. Vigorous biological activity occurs (CIPEL, 2019), and high solar radiation creates a warm layer below the air-water interface (Fairall *et al.*, 1996). Measurements were taken more than 1.5 km from the northern shore of the lake (Fig. 2b). During the measurement period, there were several short (20 min) and very short (2 min) events when the wind speed exceeded 1.5 m s^{-1}. The BLIMP imaging package simultaneously captured the corresponding development of thermal water surface patterns on a larger scale.

The transient and random nature of the contrast between smooth slicks and rippled surface areas was captured by the contrast in the BLIMP images. During the measurement campaigns, we located potentially interesting measurement areas using the infrared imagery from the BLIMP and RBG images from the ZiviCat, as well as by direct visual inspection of the state of the water surface from the accompanying boat. The ZiviCat was moved to these areas via remote control. The irregular ZiviCat tracks observed in the images (Fig. 2b, Fig. 6, Fig. 7) reflect this strategy.

RESULTS

Surfactants in the surface microlayer

Twenty-eight water sample sets were selected (surface and bulk) and separated into two groups: those coming from slick areas and those from non-slick areas. The enrichment factor was usually >1 for the smooth slicks and rippled non-slick areas (Fig. 4b, Salter, 2010). The p-value associated with the permutation test, which corresponds to the Excitation Emission Matrix (EEM) component close to 450 nm, was 0.022. This maximum, labeled P1 in Fig. 4, corresponds to classic "A" peak regions identified by Coble (1996), representing terrestrial humic substances (Murphy *et al.*, 2008). Similar results were obtained by analyzing the remaining Fluorescent Dissolved Organic Matter (FDOM) peaks (P2, P3; Fig. 4). Note that the dominant peak can be different for each sample set. For P1, the boxes for the slick and non-slick areas are clearly separate (higher p-value), whereas at P2 and P3 they overlap, and median values are no longer distinct. From the results, a systematic spatial variability of FDOM between smooth slicks and rough non-slick areas is evident, with wider scatter in the slicks (Fig. 4b). For all three peaks, the interquartile range of the slick areas is significantly larger than that of the non-slick areas.

Air-water boundary layer

On 18 April 2019, incoming solar radiation, measured by a radiometer on the stationary platform LéXPLORE (Wüest *et al.*, 2021), located ~6 km away from our study site, increased steadily throughout the morning (Fig. 5a). To calculate the heat budget, surface heat flux terms were determined based on the *in situ* ZiviCat data and the measured incoming solar radiation. The heat budget in Fig. 5a is composed of solar short-wave radiation ($Q_{sw\downarrow}$) and surface cooling which is calculated as:

$$Q_{cooling} = Q_{lw\uparrow} - Q_{lw\downarrow} + Q_{lat} + Q_{sen} \quad (1)$$

where $Q_{lw\uparrow}$ is outgoing long-wave radiation, $Q_{lw\downarrow}$ is incoming long-wave radiation, Q_{lat} is latent heat flux and Q_{sen} is sensible heat flux. We selected bulk models for the heat budget analysis (Tab. 1) based on a multi-annual two-point calibration for Lake Geneva (Rahaghi *et al.*, 2018). For roughness lengths and incoming long-wave radiation calculations, calibrated values for Lake Geneva were applied (Rahaghi *et al.*, 2018). For incoming radiation, the cloud cover fraction (C) was determined as $C = 1 - s$, where s is the ratio of the measured short-wave radiation to clear-sky short-wave radiation, which was calculated following Crawford and Duchon (1999) based on the methods of Meyers and Dale (1983). The latent and sensible heat fluxes were calculated using the Monin-Obukhov similarity the-

ory and empirical relationships by estimating turbulent stability functions and roughness lengths for wind, temperature and humidity (Zeng *et al.*, 1998; Rahaghi *et al.*, 2018). The atmospheric stability parameter was calculated as $\zeta = z/L_{MO} = 0.93$, where z is the measurement height for wind speed, and L_{MO} is the air-side Monin-Obukhov length obtained from averaged values during the entire measurement period; the Monin-Obukhov length will be discussed in the Discussion section. During the measurement period, shortwave radiation clearly dominated the surface heat budget,

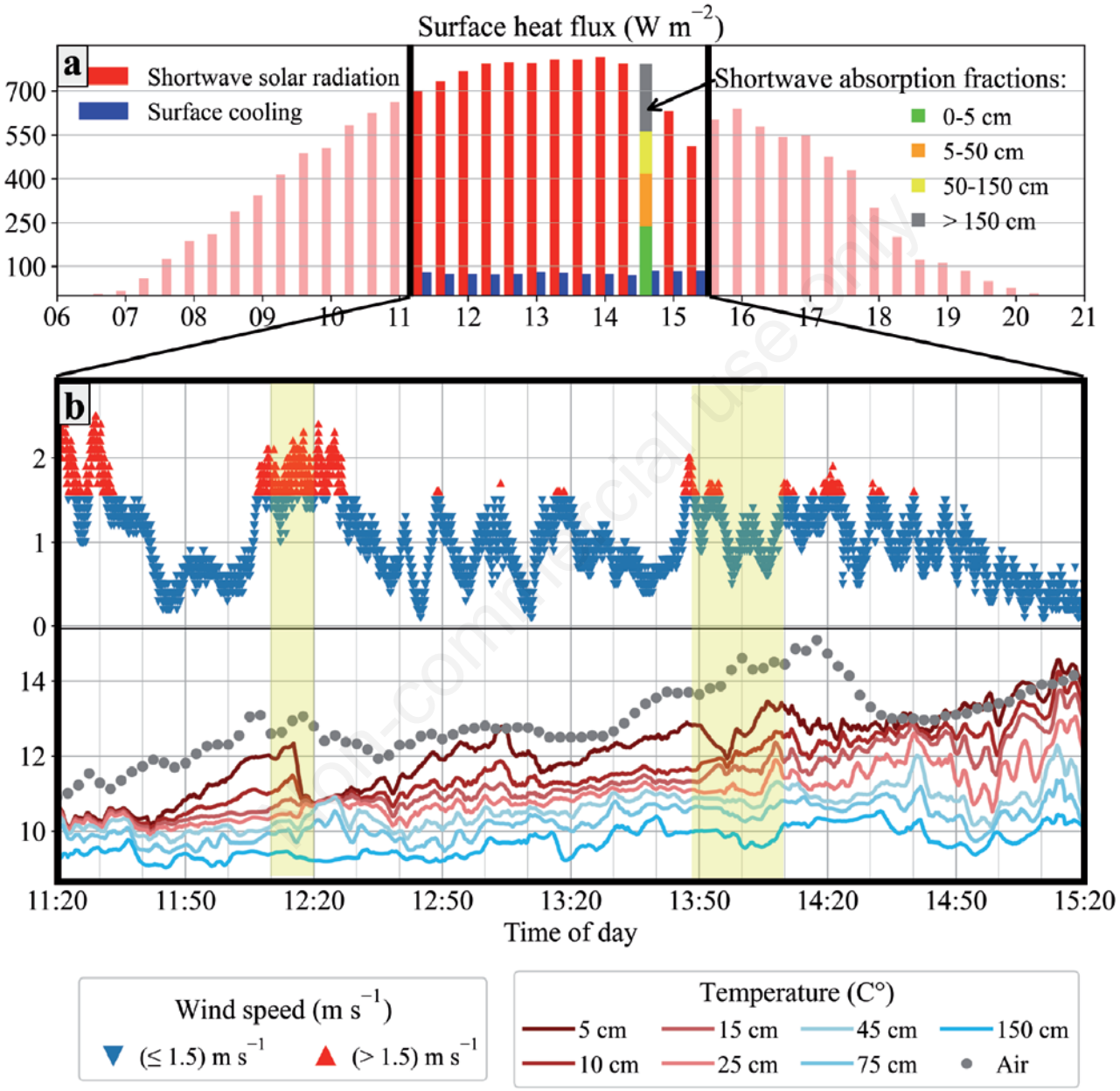

Fig. 5. Surface energy budget and observed *in situ* parameters on 18 April 2019. a) Incoming short-wave radiation (red) is compared to surface cooling (blue) due to long-wave radiation, sensible and latent heat fluxes. The diurnal variation in short-wave radiation was measured, whereas the cooling terms were calculated based on the observed parameters from 11:20 to 15:20 (local time). Outside this observation period, shortwave radiation is shown in light red. The absorption fractions of incoming short-wave radiation for different layers in the water are given at 14:30; the legend indicates the depth ranges. b) Time series of wind speed (top panel; m s^{-1}) and air temperature and near-surface water temperature (bottom panel; °C) from 11:20 to 15:20. The temperature data were smoothed using a 2-min moving average. Yellow shaded bands mark Episodes 1 and 2, respectively. Wind speeds above and below 1.5 m s^{-1} are indicated in red and blue, respectively. The legend for temperature gives the water depth of the sensor.

with surface cooling having a negligible effect under such low-wind conditions. Water surface temperatures were clearly below the air temperature (Fig. 5b). Due to the resulting downward heat flux, the near-surface water temperature increased (Fig. 5b) at all levels in the near-surface water column during the measurement period. The absorption profile of the incoming shortwave radiation in the water was estimated as:

$$f(z) = \sum_{i=1}^{n} F_i\left[1 - \exp\left(-k_{d_i} z\right)\right] \quad (2)$$

where n is the number of wavelength bands, F_i are the fractions of solar energy in each band, and k_{d_i} are the corresponding attenuation coefficients. We estimate $Q_{sw\downarrow}(z) = f(z)\, Q_{sw\downarrow}(0)$ as the amount of solar radiation absorbed down to depth z; for $Q_{sw\downarrow}(0)$, see Tab. 1. For ultraviolet and infrared bands, we used the attenuation coefficients provided by Olesen and Maberly (2001) and Jellison and Melack (1993), respectively, as summarized in Woolway *et al.* (2015). Visible light, accounting for less than half ($F_i = 0.42$) of incoming solar radiation (Gueymard *et al.*, 2002), can penetrate into deeper layers. As a result, its attenuation coefficient depends on the transparency of near-surface water. This data was not available for our field campaign; instead, hyperspectral underwater irradiance measurements made with an autonomous profiler (Minaudo *et al.*, 2021) the following year during the same period at the LéXPLORE platform were used to estimate $k_{d_{visible}}$. In the second half of April 2020, the weighted average of spectral attenuation coefficients was calculated as $\bar{k}_d = 0.45 \pm 0.05\ m^{-1}$, and was implemented in the calculations (Fig. 5a). Most of the solar radiation was ab-

Tab. 1. Bulk models for radiative, sensible, and latent heat fluxes. The calibrated values for Lake Geneva are indicated by coefficients C_i. Details are given in Rahaghi *et al.* (2018).

Surface heat flux	Formula	Reference
Incoming shortwave radiation	$Q_{sw\downarrow} = Q_{sc}F_{dir}(1 - A_{dir}) + Q_{sc}F_{diff}(1 - A_{diff})$ $F_{dir} = (1 - C)[(1 - C) + \frac{C}{2}]^{-1}$ $F_{diff} = 1 - F_{dir}$	Cogley (1979); Fink *et al.* (2014)
Incoming longwave radiation	$Q_{lw\downarrow} = \varepsilon_{atm}\sigma(T_{air} + 273.15)^4$ $\varepsilon_{atm} = 1.24\mathcal{C}_1(1 + \mathcal{C}_2\mathcal{C}^2)\left(\frac{e_a}{T_{air} + 273.15}\right)^{1/7}$ $\mathcal{C}_1 = 0.983, \mathcal{C}_2 = 0.11$	Brutsaert (1975)
Outgoing longwave radiation	$Q_{lw\uparrow} = \varepsilon_{water}\sigma(T_{water} + 273.15)^4$	-
Sensible and latent heat flux	$Q_{lat} = \rho_{az}L_v u_* q_*, Q_{sen} = \rho_{az}C_{p,a}u_* T_*$ $f_m(\zeta) = \frac{\kappa z_u}{u_*}\frac{\partial u}{\partial z}, f_e(\zeta) = \frac{\kappa z_q}{q_*}\frac{\partial q}{\partial z}, f_h(\zeta) = \frac{\kappa z_t}{T_*}\frac{\partial T}{\partial z}$ $\zeta = \frac{z}{L_{MO}} = \frac{z\kappa g\left[\frac{Q_{sen}}{C_{p,a}} + 0.61\frac{(T_{a,z} + 273.15)Q_{lat}}{L_v}\right]}{\rho_{az}u_*^3 T_v}$ $z_0 = 0.013\, u_*^2/g + \mathcal{C}_3\, \nu_a/u_*$ $z_{0q} = z_{0t} = z_0 \exp\left[-\mathcal{C}_4(u_* z_0/\nu_a)^{0.25} + 2.57\right]$ $\mathcal{C}_3 = 0.01, \mathcal{C}_4 = 1.52$	Monin and Obukhov (1954)

sorbed in the layer closest to the surface (Fig. 5a), where the temperature increase was strongest.

Two episodes of different wind conditions were investigated in detail (yellow shaded bands in Fig. 5b), hereinafter called Episode 1 and Episode 2.

Episode 1: Wind speed mostly above 1.5 m s^{-1}

During Episode 1, the ZiviCat moved continuously along the track shown in Fig. 2c. The wind speed first progressively increased and then remained just above 1.5 m s^{-1} (Fig. 6a). The wind direction remained nearly constant (onshore winds; Fig. 2c). The air temperature was higher than the LSWT (Fig. 6b). In the early stage, LSWT spatial gradients were relatively small, the near-surface water layer was strongly stratified, and there were only low amplitude swells on the surface (Fig. 6b, c). As the wind continued to blow, slick/non-slick patterns appeared on the water surface. Surface and near-surface conditions hardly changed while the ZiviCat operated inside the slick (Fig. 6d). Tracks of the ZiviCat and the boat movements, which disturbed the stratification and caused upwelling of colder water to the surface, are clearly visible. When a sharp front between the slick and a larger cold area appeared in the BLIMP thermal images, we navigated the ZiviCat towards that front (thermal contrast of up to 2°C). This thermal front coincided with a surface roughness gradient, *i.e.*, a slick/non-slick boundary. Fig. 6e shows where the ZiviCat just passed the front and entered the cold area. The very rapid drop in LSWT and near-surface water temperatures is evident in the thermal image (Fig. 6e) and the temperature time series (Fig. 6b), respectively. Simultaneously, small well-developed sharp-crested GCW appeared in the RGB image as the Zivicat entered the non-slick area (Fig. 6e). In the last panel (Fig. 6f), the ZiviCat was entirely inside the cold/rippled area. The GCW were well-developed, and the stratification in the upper 25 cm of the water column had disappeared, with temperatures in that layer below those in the warm slick (Fig. 6b, c).

The thermal images in this sequence also show the rapid time evolution of surface water temperature in response to forcing by steady winds exceeding the 1.5 m s^{-1} threshold. In the upper right and lower left sectors of the thermal images, large areas of colder water progressively expanded (Fig. 6d-f). At the same time, in the upper right sector, within the large warm slick, many small "islands" of colder water appeared almost simultaneously. They stretched in the wind direction and continuously increased in size and number within minutes (Fig. 6e, f).

Episode 2: Wind speed mostly below 1.5 m s^{-1}

After ~12:25, the wind speed remained low for 1.5 h, rarely exceeding the threshold of 1.5 m s^{-1}, and surface heating by solar radiation continued (Fig. 5). The second episode of interest occurred at ~13:50 when wind speed exceeded 1.5 m s^{-1} during two short intervals (each about 2 min) (Fig. 7a). The wind direction remained nearly constant (off shore winds; Fig. 2d). The ZiviCat continuously moved along the track indicated in Fig. 2d.

The time evolution of surface roughness, LSWT, and wind data during Episode 2 is shown in Fig. 7c-f. LSWT was almost uniform in the center of Fig. 7c, even though GCW started to form. Two brief periods of wind speeds >1.5 m s^{-1} generated wind-induced small ripples on the water surface, as seen in the RGB images (Fig. 7c, d). However, the GCW appear not to be as sharp-crested as in Fig. 6f. There was a stronger near-surface stratification compared to Episode 1 (Fig. 7b) due to continued strong solar radiation and low wind speed.

The ZiviCat then entered a cooler patch (Fig. 7d), where GCW had further developed and surface temperatures had dropped slightly (<1°C, Fig. 7b, d). However, unlike in Episode 1, in terms of both duration and wind speed, wind forcing was not enough to break up the near-surface stratification. LSWT patterns can be seen on the surface but with weaker temperature gradients than in Episode 1. Thereafter, the ZiviCat advanced into progressively warmer surface patches (Fig. 7e, f) and stratification returned to similar values as in Fig. 7c, with higher fluctuations due to the passing of a packet of what appears to be long waves generated by a passing boat (Fig. 7f).

Even after wind speeds decreased below 1.5 m s^{-1}, cooler patches are visible in the thermal images in Fig. 7d-f. Real-time monitoring of surface roughness and surface water temperature indicated that even though wind-induced GCW had disappeared rapidly (RGB images in Fig. 7e, f), the associated heterogeneity in the LSWT continued to develop and change in shape; however, at a much slower rate and with much smaller horizontal gradients than in Episode 1 (Fig. 6). A noteworthy feature at the top of the thermal images of Fig. 7e, f is the formation of long, streak-like warm structures aligned with the wind.

DISCUSSION

Our measurements were carried out under stable ABL conditions when a strong Diurnal Warm Layer (DWL) had formed near the surface, winds were light and heat flux was into the lake. Above a wind threshold of ~1.5 m s^{-1}, smooth surface slick/rough surface non-slick patterns appeared on the surface, causing well-developed Gravitational Capillary Waves (GCW) in the rough surface areas. The LSWT in these rough patches was up to 1.5°C cooler than in the surrounding smooth surface slicks with sharp temperature gradients between the two. DWL stratification disappeared in the near-surface layer of the rough patches. This led to a rapid spatial redistribution of LSWT patterns with strong horizontal thermal contrasts. Our data

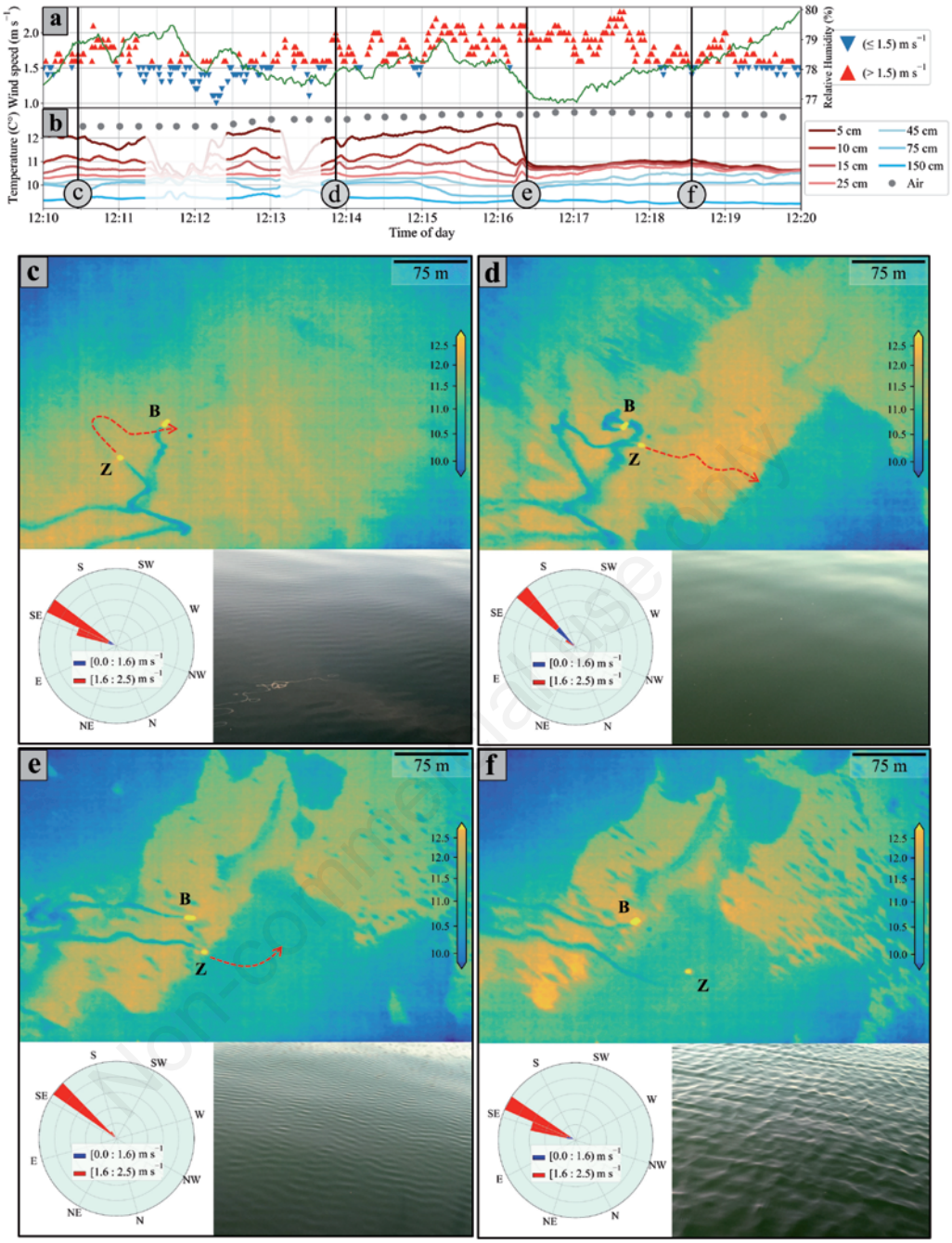

Fig. 6. Surface temperature and roughness evolution during Episode 1 with wind speed >1.5 m s^{-1}. a). Wind history and Relative Humidity (RH; green line) during this time window. b) Time series of the near-surface water temperatures at different depths and air temperature at 3-m height between 12:10 and 12:20 (local time). Two sharp temperature drops at ~12:12 and 12:13, indicated by the lighter colored segments, occurred when the ZiviCat traversed boat tracks, which had caused upwelling of cold water. c)-f) Four snapshots at different times are marked by vertical bars in a) and b). Each panel consists of (clockwise): (i) a thermal image taken by the BLIMP (top; the ZiviCat and the accompanying boat are marked with letters Z and B, respectively; the colorbar indicates water temperature in °C), (ii) a ZiviCat RGB camera image of the lake surface (bottom right), with near- and far-field distance scales of 1.2 and 4.5 m (Gerum *et al.*, 2019), respectively, and (iii) a wind rose diagram showing the wind magnitude and direction (bottom left). Wind data present one-min averages. The North on the rose diagram is aligned with the North in the IR images, and thus, the wind direction can be superimposed onto the thermal images. The tracks of the ZiviCat (Z) and the boat (B) in the thermal images are caused by upwelling of colder water (propellers at ~30-cm and ~50-cm depth, respectively). In each thermal image, the ZiviCat trajectory from one image to the next is approximated by a red dash-lined arrow. Colder upper left and lower right corners of the thermal images are artifacts (Rahaghi *et al.*, 2019c).

indicate that there was a higher surfactant concentration in smooth slicks than in rough surface areas. In the following, we will further describe the nature of the surfactant material and discuss how the interplay of surfactants, low wind, DWL formation, and GCW development affects the dynamics of the near-surface layer.

Natural surfactants

In oceanic studies, it has been shown that slicks have higher surfactant concentrations (Wurl *et al.*, 2016). However, such a study has not been carried out in a lake before. To investigate the surfactant distribution in smooth and rough areas, water samples were collected at the sur-

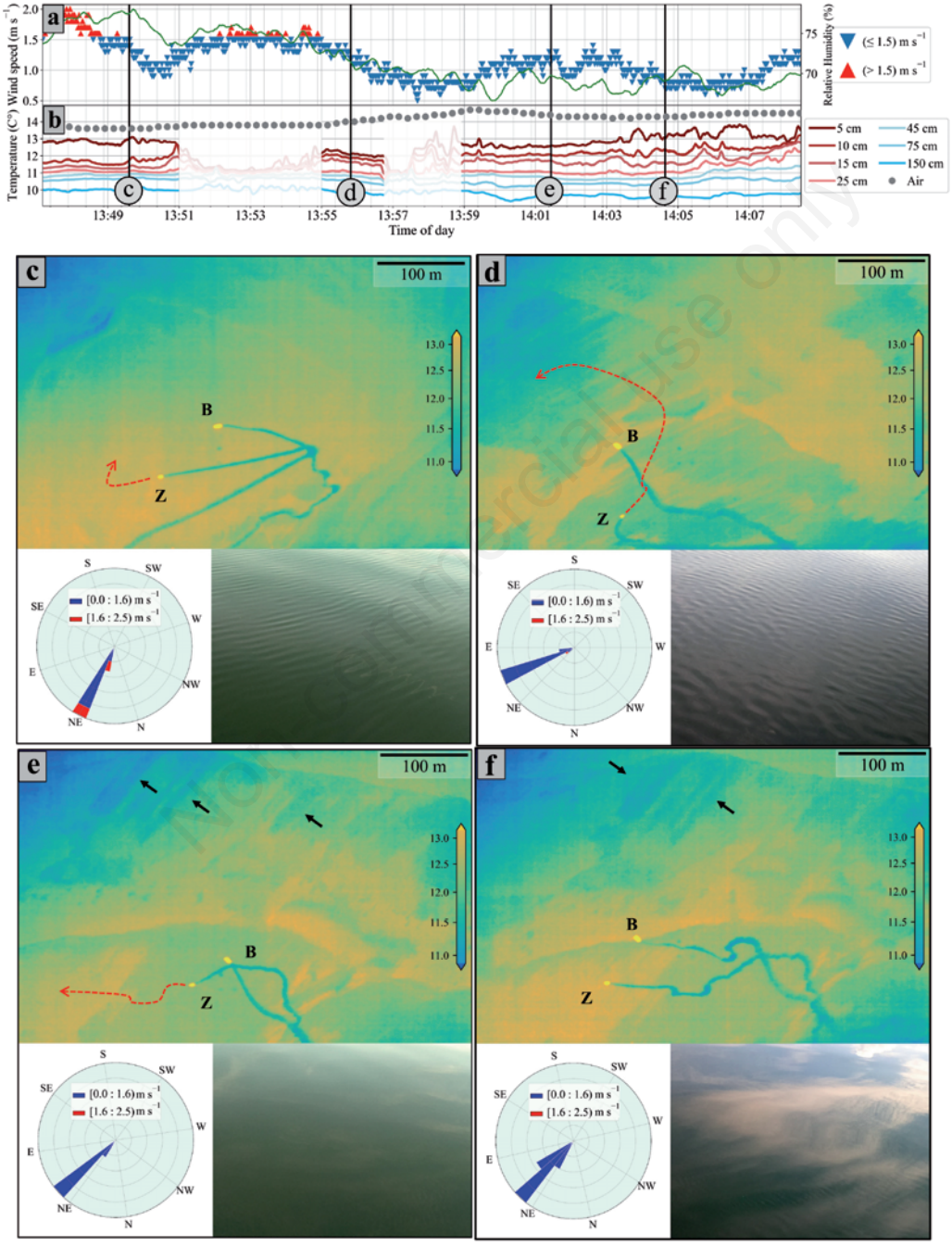

Fig. 7. Surface temperature and roughness evolution during Episode 2 at low wind speed. See the caption of Fig. 6 for details. The whitish-grayish shades on the water surface in the RGB images in e) and f) are cloud reflections on the mirror-like water surface. Black arrows in the thermal images point at long streak-like features.

face and the near-surface water layer of Lake Geneva when winds were above the threshold speed of 1.5 m s^{-1}. The samples were analyzed for the presence of surfactants. The analysis revealed that three peaks (P) frequently appeared in the Excitation Emission Matrix (EEM) (Fig. 4a). The study by Salter (2010) showed that the enrichment factors derived from these peaks strongly correlate with the EF of surfactant activity in an estuarine region during different seasons. Peak P1 corresponds to terrestrial humic substances, whereas components P2 and P3 are linked to marine and terrestrial humic materials (Murphy *et al.*, 2008) and tryptophan-like components (Wolfbeis, 1985), respectively. However, neither of these two substances shows as distinct a difference in EEM concentration between slick and non-slick areas as peak P1 does. Although the chemical composition of slicks can vary significantly spatiotemporally (Frew *et al.*, 2006), our results suggest that the Surface Micro Layer in general, and slicks, in particular, are more likely to be enriched by allochthonous production rather than by autochthonous activities (Salter, 2010), as would be expected in inland waters (Hunter and Liss, 1981). Further extensive sampling campaigns are required to map the SML composition in Lake Geneva in more detail.

The surfactant analysis of 28 water sample sets collected on four different days established that there is a significant difference in surfactant concentration between smooth slicks and rough non-slick areas, with concentrations in slicks being much higher, in agreement with observations in the ocean (Wurl *et al.*, 2016). The larger interquartile range in the slick areas (Fig. 4c) indicates higher variability in enrichment, suggesting that the thickness and characteristics of the surface surfactant film varies more within slicks than in rough surface areas. This can affect solar radiation penetration and lead to LSWT variability within warm slicks, as observed in Figs. 6 and 7. It can also affect the slick response to wind forcing by modifying dilatational viscoelasticity in the uppermost layer of the water (Frew, 1997). Thinner surfactant layers may break up more easily under wind forcing and open up rough non-slick areas within slicks (Fig. 6f). Previous studies in the ocean also observed a wider interquartile range inside slicks (Wurl *et al.*, 2016). During our water sampling campaigns, direct visual observations of the lake surface confirmed that smooth surfaces can be associated with surfactant-enriched slicks. Thus, the results of the surfactant study allow us to interpret the observed surface roughness in the RGB lake surface images taken by the ZiviCat on 18 April 2019 (Figs. 6, 7) in terms of surfactant concentration.

Diurnal Warm Layer (DWL)

The meteorological conditions on 18 April 2019 were characterized by weak winds and a significant input of solar radiation into the upper layer of the lake (Fig. 5a). For the surface heat flux, incoming solar radiation substantially exceeds cooling (Eq. (1), Fig. 5a). This situation leads to the formation of a Diurnal Warm Layer (DWL) (Price *et al.*, 1986). Under calm conditions (wind speed below 1.5 m s^{-1}) and intense incoming shortwave radiation (clear skies), DWL amplitudes in tropical oceans and lakes may reach up to several degrees (Ward, 2006; Augusto-Silva *et al.*, 2019; Bartosiewicz *et al.*, 2019; MacIntyre *et al.*, 2021a) confined to a shallow surface layer (O(1 m)) at around midday (Gentemann *et al.*, 2009). If wind speed increases slightly, the development of GCW and the resulting surface mixing contribute to a rapid and strong reduction in diurnal warming amplitude (Gentemann and Minnett, 2008).

During Field Campaign 2, the development of a DWL was confirmed from the analysis of the heat flux terms (Fig. 5a). As a typical example, the absorption fractions of incoming short-wave radiation in different layers of the water column were calculated for light-wind conditions at ~14:30 using attenuation coefficients from Woolway *et al.* (2015) (Fig. 5a) for infrared and ultraviolet bands and the estimated k_d for Lake Geneva for the visible range. Nearly 75% of short-wave radiation is absorbed in the uppermost 1.5 m of the water column, and a large part of that in the uppermost 5 cm. Since heat absorption in this 5-cm layer is significantly greater than surface cooling, an intense, stable near-surface stratification develops. Although the rise in LSWT can potentially enhance surface cooling by increasing outgoing longwave radiation and latent heat flux (Rahaghi *et al.*, 2019a), the persistent, intense solar radiation maintains the near-surface water stratification. These high-resolution stratification profile measurements in the near-surface layer, which allowed quantification of the DWL development, are the first-ever taken in a slick study. In previous oceanic studies, water surface temperatures were compared only to one temperature measured deeper in the water column (Marmorino and Smith, 2006). The surface heat budget analysis in Fig. 5 suggests that DWL formation began earlier in the morning. However, the meteorological parameters needed to assess surface cooling were not available before 11:20.

Threshold wind speed

One of the objectives of this study was to investigate the effect of increasing wind speed on slick formation and on the dynamics of the diurnal warm layer. An analysis of all the data collected on 18 April 2019 reveals that whenever the wind speed exceeded a threshold, the near-surface stratification was altered, and patches of GCW were produced, causing mixing. Based on the ZiviCat weather station data measured 3 m above the water surface, we compared the results of Episodes 1 and 2 (respectively, Fig. 6 and Fig. 7) and determined a threshold

value of U ≈ 1.5 m s^{-1}, above which GCW start to grow. This value is close to the range (1.6 to 1.8 m s^{-1}) observed in a laboratory study (Donelan and Plant, 2009). Gentemann and Minnett (2008) reported that the DWL development in the ocean significantly changes when wind speed exceeds 1.5 m s^{-1}. The threshold also depends on wind gustiness and fetch, ABL stability, water temperature, and surface film concentration. Note that when this threshold wind speed was exceeded, the lake surface became patchy. However, warm patches (slicks) with no GCW still covered a significant part of the lake surface (Fig. 6). When winds blow above the threshold wind speed for extended periods, the area covered by smooth slicks becomes progressively smaller (Fig. 1).

Wave height estimate

The non-slick area (Fig. 6f) is characterized by sharp-crested and well-developed GCW. GCW wave height can be estimated during Episode 1 based on significant wave height parameterization (Taylor and Yelland, 2001; Wang *et al.*, 2017):

$$H_s = 0.018U_{10n}^2\ (1 + 0.015U_{10n}) \quad (3)$$

where H_s is significant wave height, and U_{10n} is 10-m height neutral wind speed. Using the same parameterization scheme as for calculating the heat budget (averaged meteorological measurements over the first episode), we estimated a wave height $H_s \approx 4.4$ cm. Although the above equation was derived mainly for higher wind speeds, the resulting wave height is in the range of wave height estimates obtained from ZiviCat RGB images in Fig. 6f and visual inspection of the lake surface in the non-slick areas.

Episode 1:
Wind speed above the 1.5 m s^{-1} threshold

In Episode 1, the most striking feature of the LSWT field was the sharp drop in stratification when moving from a slick to a non-slick area (Fig. 6e). Using one-min averaged temperature data from the uppermost 25 cm of the water column, the buoyancy frequency (N) can be estimated. Just before entering the rough rippled area (at ~12:16), a value of $N = 9.21\times10^{-3}\ s^{-1}$ (~33 cycles per hour) was found. Stratification of this intensity is comparable to previous measurements in lakes under surface heating and low wind conditions (Augusto-Silva *et al.*, 2019; Bartosiewicz *et al.*, 2019). In the non-slick area (at ~12:18), the buoyancy frequency dropped to less than one cycle per hour. The strong horizontal LSWT gradient (1.5°C in 10 m; estimated by combining temperature data in Fig. 6b and ZiviCat speed) between ~12:16 and ~12:17 can be explained by a sequence of two processes: (i) preferential absorption of shortwave solar radiation in the water column causes significant temperature gradients in a very thin layer below the surface, as discussed above (Fig. 5a), and (ii) air-water momentum exchange increases substantially as GCW form due to the potentially significant contribution of the wave-form drag in momentum transfer compared to the background tangential skin friction (Banner and Peirson, 1998).

Frew (1997) reported that surface film-induced non-zero viscoelasticity can modify this surface exchange by dampening small waves or by changing the near-surface turbulence. Here, the observed effect of surfactant concentration is mostly associated with the former. Within slicks, wind-wave formation and growth are suppressed (most likely due to higher surfactant concentrations; Fig. 4b), resulting in the absence of wave-induced mixing, which causes less efficient near-surface mixing than in non-slick areas. In particular, under low wind conditions, turbulence production by wave-induced motions exceeds that resulting from wind-driven shear (Savelyev *et al.*, 2020). The enhanced wave-induced mixing in non-slick regions can partly be attributed to the generation of small-scale (centimeter-scale) Langmuir circulation at the onset of wind-wave development (Veron and Melville, 2001; Tejada-Martínez *et al.*, 2020). In their laboratory experiments, Veron and Melville (2001) demonstrated that adding surfactants prevents wave formation and thus the generation of this small-scale circulation. The total wind stress increases as the wave field develops outside the slicks (Banner and Peirson, 1998). This effect can be seen as reduced wind drag (Shen *et al.*, 2019; Vanderplow *et al.*, 2020), and smaller stress exerted by the airflow (Benetazzo *et al.*, 2019) inside slicks. Therefore, slicks can be expected to remain warmer than non-slick areas under strong solar radiation and low wind conditions. As a result, slicks can alter the dynamics of the air-water interface, causing spatial variability of LSWT between slicks and non-slick areas.

During Episode 1, a rapid transition from the warm stratified slick to a cold non-stratified non-slick area takes place over a distance of less than 10 m, as is evident from the destratification of the upper 25 cm of the water column and a more than 1.5°C drop in the subskin temperature (Fig. 6b). The Monin-Obukhov length scale (L_{MO}) illustrates the balance between stabilizing buoyancy forces and Turbulent Kinetic Energy (*TKE*) produced by wind-induced mixing ($u_{*,\mathrm{water}}$) under horizontally homogeneous and stationary conditions and ignoring shear- or wave-driven turbulence (Thompson *et al.*, 2019). This scaling is given by:

$$L_{MO} = \frac{u_{*,water}^3}{\kappa B} \quad (4)$$

where κ = 0.41 is the von Karman constant and B is the effective buoyancy flux. Tab. 2 lists the parameters used

to calculate L_{MO} together with their associated definitions. Following the methods outlined in the heat budget analysis (Fig. 5a), correcting for stability of the atmospheric boundary layer and measurement height, and using 5-min averaged data, L_{MO} was estimated as ~5 cm for the non-slick area in Episode 1. This small L_{MO} value is the result of a large B (Fig. 5) and a weak $u_{*,\mathrm{water}}$ value. However, this estimate should be interpreted with caution, because the assumptions of horizontal homogeneity and stationary conditions may not be satisfied in the present case due to the observed patchiness (Figs. 6, 7) which can affect B and $u_{*,\mathrm{water}}$. Small ratios between L_{MO} and the actively mixing layer depth (~ 25 cm in the non-slick area in Episode 1; Figure 6b), previously observed (Augusto-Silva *et al.*, 2019; MacIntyre *et al.*, 2021a), imply that wind-induced shear dominates turbulence production only in shallow surface layers. On the other hand, wave-induced mixing can contribute significantly to TKE production even under non-breaking surface waves (Qiao *et al.*, 2016; Savelyev *et al.*, 2020).

Therefore, we investigated the mixing time that can be estimated from wave-induced turbulence production in the near-surface layer. Dai *et al.* (2010) determined the water-side eddy diffusivity induced by low amplitude mechanically-generated non-breaking surface waves. In their laboratory experiment, a wave amplitude of 1.5 cm generated a turbulent diffusivity K_z of O (10^{-4} m^2 s^{-1}) in the near-surface layer. Applying this diffusivity to the present case, a time scale (h^2_{mix}/K_z) of ~10 min is obtained. Dai *et al.* (2010) also reported that with increasing wave amplitude, this time scale rapidly decreases while the mixing rate and the mixing depth increase. Consequently, the actual time in Episode 1 would be shorter since wave amplitudes are greater, which is also evident from the LSWT time evolution in Fig. 6c-f. Babanin and Haus (2009) measured turbulent dissipation below similar non-breaking laboratory waves. They observed that although turbulence was highly intermittent in space and time, turbulent dissipation rates reached values comparable to those reported under breaking waves. They indicated that the turbulent dissipation rate is very sensitive to wave amplitude, since it increases with the third power of wave amplitude. The above estimates suggest that the strong and rapid mixing in the rough non-slick areas observed in our study, is predominately produced by the presence of GCW and that wind stress-induced TKE in the near surface layer, estimated by L_{MO}, only makes a minor contribution. Furthermore, under stable ABL and low wind conditions, the drag coefficient is considerably smaller than in neutral and unstable cases (Smith, 1988; Kara *et al.*, 2005). This results in low $u_{*,\mathrm{water}}$ and wind-induced TKE levels, thus underscoring the importance of wave-induced mixing under these conditions.

Given the above timescale, it can be expected that the water surface layer in the non-slick area reaches quasi-equilibrium within minutes after the wind speed threshold is exceeded, and surface waves are formed. The relatively constant LSWT observed in the non-slick region (12:17 to ~12:25) during the period when the wind speed was above the threshold further supports this. The results confirm that the diurnal warming amplitude rapidly changes in response to slight variations in wind speed when GCW develop in the absence of surfactants and cause near-surface mixing (Gentemann and Minnett, 2008). The time evolution of the thermal contrast between slick and non-slick areas (Fig. 6d-f) that appeared shortly after the wind speed exceeded the threshold illustrates that, at low wind speeds, the near-surface layer is particularly sensitive to wind speed changes.

The scenario described above for Episode 1 in Lake Geneva is different from previous observations in the ocean that reported slightly colder (<0.5°C) surface temperatures in slicks (*e.g.*, Frew *et al.,* 2004, Marmorino and Smith, 2006 and references given therein). Those ocean measurements were carried out under upward heat fluxes and thus unstable ABL conditions, whereas our measurements were taken under stable conditions ($\zeta = 0.93$) and net surface warming (Fig. 5a), which is typical for the spring period over Lake Geneva (Rahaghi *et al.,* 2019b). The difference between our measurements and those carried out in the ocean illustrate two mechanisms through which slicks can affect the surface water temperature: In the ocean studies, the reduction of temperature in slicks was associated with the surfactants' ability to suppress

Tab. 2. Parameters used for the water-side Monin-Obukhov length scale and mixing time scale calculations.

Parameter	Definition	Computed value
$u_{*,water}$	$\left(\frac{\rho_a}{\rho_w}\right)^{\frac{1}{2}} u_{*,air}$ [(a)]	0.0014 [$m\ s^{-1}$]
B	$\frac{g\alpha}{\rho_w c_p} Q^*_{Net}$ [(b)]	1.45×10^{-7} [$m^2\ s^{-3}$]

[(a)] The air-side friction velocity is calculated following Zeng et al. (1998), accounting for atmospheric boundary layer stability and measurement height; [(b)] The effective heat flux considers only that amount of shortwave radiation (mainly in the visible part) that heats the actively mixing layer (estimated to be 25 cm based on thermistor measurements, Fig. 6b; Imberger, 1985; Thompson et al., 2019). The remaining terms in the surface heat budget are not affected.

convective motions close to the surface by thickening the water-side viscous sublayer (Bower and Saylor, 2011). Therefore, cooled surface water could not be exchanged efficiently with warmer sub-surface water. In the present study, however, under net surface warming, the slick *vs.* non-slick temperature difference changed both in sign and intensity. Furthermore, surfactants inhibited mixing in slicks by suppressing the wind-wave formation and dampening short GCW amplitudes. Thus, the elevated surface water temperature due to the DWL effect was maintained, at least temporarily, inside slicks. This finding indicates that the impact of slicks on surface water temperature depends on: (i) the direction of air-water heat transfer, (ii) the intensity and duration of solar radiation and wind forcing, (iii) characteristics of the GCW field, and (iv) the type of the material inside slicks, as well as the presence of biological activity (Wurl *et al.*, 2018).

The thermal images in Fig. 6, particularly those captured at the later stages of LSWT development with winds above the 1.5 m s^{-1} threshold, showed sequentially arranged warm and cold patches, elongated in the wind direction. The elongation of all surface patches in the wind direction suggests that wind shear is the driving force in these dynamics. In particular, one can identify multiple islands of cold water that develop simultaneously over a large area inside a large warm slick (right-hand side of Fig. 6f). All these features rapidly evolve in time, with cold surface areas overall increasing in size. The LSWTs in these cold areas are comparable to those measured with the ZiviCat (Fig. 6f), suggesting that they can be characterized by well-developed GCW and a near-surface destratification. Thus, air-water exchange processes can be expected to change strongly and rapidly with time and space, even under light winds. Considering the larger interquartile range observed in the slick areas (Fig. 4c), it is likely that the observed simultaneous development of these islands of cold water was mainly due to the spatial heterogeneity in the thickness or composition of surfactant enrichment rather than to small-scale spatial variations in the wind field. Marmorino and Smith (2006) reported that the ocean slick they studied did not change much over time.

Episode 2:
Wind speed below the 1.5 m s^{-1} threshold

In Episode 2 (Fig. 7), the period during which the wind speed exceeded the threshold was much shorter than in Episode 1 and lasted only about 2-min. Nevertheless, a drop in surface temperature was observed inside the rippled water surface area shortly after the second slight increase in wind (Fig. 7b-d), although with much smaller amplitudes, barely affecting the near-surface stratification. In Fig. 7b, the topmost temperature sensor (depth of about 5 cm) shows a noticeable decrease (<1°C) after the two very short wind events impacted on the surface (Fig. 7a). However, the second and third top thermistor measurements (Fig. 7, depths of ~ 10 and 15 cm) revealed no signs of mixing due to the absence of sufficient wind stress, indicating that wind-induced mixing probably only affected the uppermost centimeters of the near-surface water layer (which could not be captured by our measurement system). This agrees with the findings of Dai *et al.* (2010) concerning the dependence of penetration depth on wave height. Despite the brief appearance of smooth and rough surfaces caused by that short wind pulse, the corresponding spatial variability in the surface temperature persisted over an extended period (Fig. 7e, f). Length and time scales were not calculated for Episode 2 because the event was shorter than the timescale related to such a development, and GCW did not fully develop.

Elongated streak-like warm features appeared in the thermal imagery, aligned with the wind (*e.g.*, black arrows in Fig. 7e, f). Marmorino *et al.* (2008) observed that striped patterns had formed on the upwind side of slicks aligned with wind direction. They suggested that Langmuir circulation (with a spacing of ~25 m) that developed under steadily increasing wind (up to 5 m s^{-1}) plays a major role in fragmenting slicks, with surface film cumulating in the convergent zones. A similar process for redistributing biogenic films was proposed by Ermakov (2018) who observed the formation of streaks on the upwind side of artificial slicks under higher wind conditions (8 m s^{-1}) with cross-wind scales of 7-10 m. Although the spatial scales (~10 to 20 m) in our observations are similar to the above studies, the formation of Langmuir cells is unlikely for such short-duration, low wind speed events (<2.5 m s^{-1}). Even if a uniform wind field over the area of the thermal images (Fig. 7c-f) were present, the conditions required for their formation would not be fulfilled (Leibovich, 1977). Warm streaks were previously observed under light wind conditions in Lake Geneva (Rahaghi *et al.*, 2019a), where ZiviCat measurements showed that warm near-surface water underwent downwelling to more than 1.5 m depth in those streaks. Large-scale upwelling and downwelling processes below the surface may also manifest themselves by streak-like features on the surface. Farrar *et al.* (2007) showed that internal waves under low wind speeds and intense solar radiation can cause similar surface temperature patterns at these scales, which favor the development of a DWL. Additional investigations with targeted measurement campaigns are needed to determine the origin and dynamics of these streaks and their role in near-surface layer dynamics.

Lemmin and D'Adamo (1996) reported that wind speed in Lake Geneva is less than 4 m s^{-1} 80-90% of the time during the stratification period (May to October), and winds below 3 m s^{-1} by far dominate the annual wind rose pattern (CIPEL, 2019). Rahaghi *et al.* (2019b) and Lemmin (2020) showed that the ABL is stable for the period from March to the beginning of August, at least during the daytime. The

findings of the present study are therefore an important contribution to the understanding of the annual air-water exchange cycle. Furthermore, images regularly recorded with the remote sensing camera installation (Fig. 1) confirmed that slicks are frequent during periods of stable ABL conditions. The results of the two episodes in the present study, therefore, can be considered representative for patch dynamics and air-water exchange under strong solar radiation and low wind speeds in Lake Geneva, and probably in other lakes under similar conditions.

SUMMARY AND CONCLUSIONS

This field study carried out in Lake Geneva investigated, in a novel approach, processes that can cause nonuniformity in Lake Surface Water Temperature (LSWT) under commonly occurring light wind conditions and determined how this nonuniformity can be related to biogenic surfactant distribution. High-resolution measurements of surface temperature, near-surface water temperature profiles and real-time observations of surface roughness were combined. Surfactant concentrations are significantly lower in rough non-slick patches than in smooth slicks, as determined from field observations and Enrichment Factor (EF) analyses. Such measurements taken under stable Atmospheric Boundary Layer (ABL) conditions have not been previously reported for inland waters, in this case a lake, even though they are key for better understanding and quantifying air-water exchange dynamics.

The data show that a Diurnal Warm Layer (DWL) developed in the near-surface water column when intense solar radiation input greatly exceeded heat loss from the lake under stable ABL conditions. Under calm conditions with wind speeds below a threshold of ~ 1.5 m s^{-1}, it is evident from surface images that the surface is essentially smooth, and LSWTs vary only slightly. Stratification with a strong temperature gradient (up to a few degrees) develops in the near-surface water column with the greatest thermal gradient being in the very shallow (a few centimeters) near-surface layer.

It was demonstrated that when light (<2.5 m s^{-1}) winds rose above the threshold of ~1.5 m s^{-1}, smooth surface slick/rough surface non-slick patterns appeared on the surface, causing well-developed Gravitational Capillary Waves (GCW) to develop in the rough surface areas, thereby promoting near-surface water mixing. The LSWT in these rough patches was up to 1.5°C cooler than in the surrounding smooth surface slicks with sharp temperature gradients between the two. However, as wind continued to blow above the threshold, slicks broke up on certain parts of the surface and remained intact elsewhere; this may be due to the observed surfactant concentration variability. This led to a rapid spatial redistribution of LSWT patterns with strong horizontal thermal contrasts. The elongation of all rough surface patches in the wind direction suggests that wind shear is the driving force in the break-up of smooth slicks. It can be assumed that the time-integrated effects of the interaction between light winds and spatially varying natural films contribute to the spatial heterogeneity of LSWT and thus affect the spatial distribution of the exchange of heat, momentum and mass.

These lake observations contrast with results from previous oceanic studies where slicks were found to be cooler (<0.5°C) than ambient surface areas under net surface cooling conditions. The present results suggest that the effect of natural films on surface water temperature development depends on the direction of the heat flux (downward in the present study *vs.* upward in ocean observations reported in the literature), as well as the time evolution of near-surface processes involved in the surface renewal and turbulent heat exchange. Most previous slick studies in oceans investigated the influence of surfactants on near-surface turbulence, where reduced convective motions decreased the renewal of relatively cold surface water. Our study, carried out in a lake, highlighted the role of surfactants in retarding and dampening GCW, which is another mechanism through which slicks can affect surface water temperature.

In conclusion, the effect of high concentrations of natural surfactants on LSWT depends on atmosphere-water boundary layer dynamics. The results of the present study contribute to the understanding and the quantification of air-water exchange processes, which presently are lacking for stable Atmospheric Boundary Layer (ABL) conditions in lakes, and can be expected to be applicable to other lakes under similar boundary layer conditions.

ACKNOWLEDGMENTS

This work was supported by the Swiss National Science Foundation (SNSF) Grant No. 178866. We would like to thank Florian Breider (Central Environmental Laboratory, CEL, EPFL) for making available the Fluorescence Spectrometer and for guidance in the laboratory analysis. We also thank the EPFL Limnology Center for providing solar irradiance data from the LéXPLORE platform. The support of several colleagues for fieldwork and technical issues is greatly appreciated, specifically Htet Kyi Wynn, Benjamin Daniel Graf, Abolfazl Irani Rahaghi, and Mahmood Hamze-Ziabari. We thank the reviewers for their constructive comments.

REFERENCES

Alpers W, 1985. Theory of radar imaging of internal waves. Nature 314:245–247.

Alpers W, Hühnerfuss H, 1989. The damping of ocean waves by surface films: A new look at an old problem. J. Geophys. Res. 94(C5):6251–6265.

Augusto-Silva PB, MacIntyre S, Moraes Rudorff C de, Cortés A, Melack JM, 2019. Stratification and mixing in large floodplain lakes along the lower Amazon River. J. Great Lakes Res. 45:61–72.

Babanin AV, Haus BK, 2009. On the existence of water turbulence induced by nonbreaking surface waves. J. Phys. Oceanogr. 39:2675–2679.

Banner ML, Peirson WL, 1998. Tangential stress beneath wind-driven air-water interfaces. J. Fluid Mech. 364:115–145.

Barry DA, Liardon J-L, Paccaud P, Klaus P, Shaik N, Rahaghi AI, Zulliger L, Béguin J, Geissmann B, Tulyakov S, Ivanov A, Wynn H, *et al.*, 2019. A low-cost, autonomous mobile platform for limnological investigations, supported by high-resolution mesoscale airborne imagery. PLOS ONE 14:e0210562.

Bartosiewicz M, Przytulska A, Deshpande BN, Antoniades D, Cortes A, MacIntyre S, Lehmann MF, Laurion I, 2019. Effects of climate change and episodic heat events on cyanobacteria in a eutrophic polymictic lake. Sci. Total Environ. 693:133414.

Benetazzo A, Cavaleri L, Ma H, Jiang S, Bergamasco F, Jiang W, Chen S, Qiao F, 2019. Analysis of the effect of fish oil on wind waves and implications for air-water interaction studies. Ocean Sci. 15:725–743.

Bower SM, Saylor JR, 2011. The effects of surfactant monolayers on free surface natural convection. Int. J. Heat Mass Transf. 54:5348–5358.

Brutsaert W, 1975. On a derivable formula for long-wave radiation from clear skies. Water Resour. Res. 11:742–744.

Calamita E, Piccolroaz S, Majone B, Toffolon M, 2021. On the role of local depth and latitude on surface warming heterogeneity in the Laurentian Great Lakes. Inland Waters 11:208–222.

Cheng J, Cheng X, Meng X, Zhou G, 2019. A monte carlo emissivity model for wind-roughened sea surface. Sensors 19:2166.

CIPEL, 2019. Rapports Sur Les Études et Recherches Entreprises Dans Le Bassin Lémanique, Campagne 2018. Commission internationale pour la protection des eaux du Léman (CIPEL), Nyon, Switzerland: 303 pp.

Coble PG, 1996. Characterization of marine and terrestrial DOM in seawater using excitation-emission matrix spectroscopy. Mar. Chem. 51:325–346.

Cogley JG, 1979. The albedo of water as a function of latitude. Mon. Weather Rev. 107:775–781.

Crawford TM, Duchon CE, 1999. An improved parameterization for estimating effective atmospheric emissivity for use in calculating daytime downwelling longwave radiation. J. Appl. Meteorol. Climatol. 38:474–480.

Cunliffe M, Engel A, Frka S, Gašparović BŽ, Guitart C, Murrell JC, Salter M, Stolle C, Upstill-Goddard R, Wurl O, 2013. Sea surface microlayers: A unified physicochemical and biological perspective of the air-ocean interface. Prog. Oceanogr. 109:104–116.

Cunliffe M, Wurl O, 2014. Guide to Best Practices to Study the Ocean's Surface. Marine Biological Association of the United Kingdom for SCOR, Plymouth: 118 pp.

Dabuleviciene T, Kozlov IE, Vaiciute D, Dailidiene I, 2018. Remote sensing of coastal upwelling in the south-eastern Baltic Sea: Statistical properties and implications for the coastal environment. Remote Sens. 10:1752.

Dai D, Qiao F, Sulisz W, Han L, Babanin A, 2010. An experiment on the nonbreaking surface-wave-induced vertical mixing. J. Phys. Oceanogr. 40:2180–2188.

De Santi F, Luciani G, Bresciani M, Giardino C, Lovergine FP, Pasquariello G, Vaiciute D, De Carolis G, 2019. Synergistic use of synthetic aperture radar and optical imagery to monitor surface accumulation of cyanobacteria in the Curonian Lagoon. J. Mar. Sci. Eng. 7:461.

Donelan MA, Plant WJ, 2009. A threshold for wind-wave growth. J. Geophys. Res. 114:C07012.

Engel A, Bange HW, Cunliffe M, Burrows SM, Friedrichs G, Galgani L, Herrmann H, Hertkorn N, Johnson M, Liss PS, Quinn PK, Schartau M, *et al.*, 2017. The ocean's vital skin: Toward an integrated understanding of the sea surface microlayer. Front. Mar. Sci. 4:165.

Ermakov S, Lavrova O, Kapustin I, Ermoshkin A, Molkov A, Danilicheva O, 2018. On the "comb" structure of the edges of slicks on the sea surface. Sovrem. Probl. Distantsionnogo Zondirovaniya Zemli Iz Kosmosa 15:208–217.

Fairall CW, Bradley EF, Godfrey JS, Wick GA, Edson JB, Young GS, 1996. Cool-skin and warm-layer effects on sea surface temperature. J. Geophys. Res. Oceans 101:1295–1308.

Farrar JT, Zappa CJ, Weller RA, Jessup AT, 2007. Sea surface temperature signatures of oceanic internal waves in low winds. J. Geophys. Res. Oceans 112, C06014.

Fink G, Schmid M, Wahl B, Wolf T, Wüest A, 2014. Heat flux modifications related to climate-induced warming of large European lakes. Water Resour. Res. 50:2072–2085.

Frew NM, 1997. The role of organic films in air-sea gas exchange, p. 121–172 In: Liss PS and RA Duce (eds.), The Sea Surface and Global Change, Cambridge: Cambridge University Press.

Frew NM, Bock EJ, Schimpf U, Hara T, Haußecker H, Edson JB, McGillis WR, Nelson RK, McKenna SP, Uz BM, Jähne B, 2004. Air-sea gas transfer: Its dependence on wind stress, small-scale roughness, and surface films. J. Geophys. Res. 109:C08S17.

Frew NM, Nelson RK, Johnson CG, 2006. Sea slicks: variability in chemical composition and surface elasticity, p. 45–56 In: Gade M, H Hühnerfuss, and GM Korenowski (eds.), Marine Surface Films: Chemical Characteristics, Influence on Air-Sea Interactions and Remote Sensing, Berlin: Springer.

Frew NM, Nelson RK, McGillis WR, Edson JB, Bock EJ, Hara T, 2002. Spatial variations in surface microlayer surfactants and their role in modulating air-sea exchange, p. 153–159 In: Donelan MA, WM Drennan, ES Saltzman, and R Wanninkhof (eds.), Gas Transfer at Water Surfaces, Washington, D.C.: American Geophysical Union (AGU).

Gade M, Hühnerfuss H, Korenowski G, editors, 2006. Marine Surface Films: Chemical Characteristics, Influence on Air-Sea Interactions and Remote Sensing. Springer, Berlin: 341 pp.

Garabetian F, Romano J-C, Paul R, Sigoillot J-C, 1993. Organic matter composition and pollutant enrichment of sea surface microlayer inside and outside slicks. Mar. Environ. Res. 35:323–339.

Garbe CS, Schimpf U, Jähne B, 2004. A surface renewal model to analyze infrared image sequences of the ocean surface for the study of air-sea heat and gas exchange. J. Geophys. Res. 109:C08S15.

Gentemann CL, Minnett PJ, 2008. Radiometric measurements of ocean surface thermal variability. J. Geophys. Res. Oceans 113:C08017.

Gentemann CL, Minnett PJ, Ward B, 2009. Profiles of ocean surface heating (POSH): A new model of upper ocean diurnal warming. J. Geophys. Res. 114:C07017.

Gerum RC, Richter S, Winterl A, Mark C, Fabry B, Le Bohec C, Zitterbart DP, 2019. CameraTransform: A Python package for perspective corrections and image mapping. SoftwareX 10:100333.

Gove JM, Whitney JL, McManus MA, Lecky J, Carvalho FC, Lynch JM, Li J, Neubauer P, Smith KA, Phipps JE, Kobayashi DR, Balagso KB, *et al.*, 2019. Prey-size plastics are invading larval fish nurseries. Proc. Natl. Acad. Sci. U. S. A. 116:24143–24149.

Gueymard CA, Myers D, Emery K, 2002. Proposed reference irradiance spectra for solar energy systems testing. Sol. Energy 73:443–467.

Hamze-Ziabari SM, Razmi AM, Lemmin U, Barry DA, 2022. Detecting submesoscale cold filaments in a basin-scale gyre in large, deep Lake Geneva (Switzerland/France). Geophys. Res. Lett. 49:e2021GL096185.

Hughes PJ, Bourassa MA, Rolph JJ, Smith SR, 2012. Averaging-related biases in monthly latent heat fluxes. J. Atmospheric Ocean. Technol. 29:974–986.

Hunter KA, Liss PS, 1981. Organic sea surface films, p. 259–298 In: Duursma EK and R Dawson (eds.), Marine Organic Chemistry, Amsterdam: Elsevier.

Imberger J, 1985. The diurnal mixed layer. Limnol. Oceanogr. 30:737–770.

Jarvis NL, 1962. The effect of monomolecular films on surface temperature and convective motion at the water/air interface. J. Colloid Sci. 17:512–522.

Jellison R, Melack JM, 1993. Meromixis in hypersaline Mono Lake, California. 1. Stratification and vertical mixing during the onset, persistence, and breakdown of meromixis. Limnol. Oceanogr. 38:1008–1019.

Kara AB, Hurlburt HE, Wallcraft AJ, 2005. Stability-dependent exchange coefficients for air–sea fluxes. J. Atmospheric Ocean. Technol. 22:1080–1094.

Karimova S, 2012. Spiral eddies in the Baltic, Black and Caspian seas as seen by satellite radar data. Adv. Space Res. 50:1107–1124.

Kawai Y, Wada A, 2007. Diurnal sea surface temperature variation and its impact on the atmosphere and ocean: A review. J. Oceanogr. 63:721–744.

Kujawinski EB, Farrington JW, Moffett JW, 2002. Evidence for grazing-mediated production of dissolved surface-active material by marine protists. Mar. Chem. 77:133–142.

Kurata N, Vella K, Hamilton B, Shivji M, Soloviev A, Matt S, Tartar A, Perrie W, 2016. Surfactant-associated bacteria in the near-surface layer of the ocean. Sci. Rep. 6:19123.

Leibovich S, 1977. On the evolution of the system of wind drift currents and Langmuir circulation in the ocean. Part 1. Theory and averaged current. J. Fluid Mech. 79:715–743.

Lemmin U, 2020. Insights into the dynamics of the deep hypolimnion of Lake Geneva as revealed by long-term temperature, oxygen, and current measurements. Limnol. Oceanogr. 65:2092–2107.

Lemmin U, D'Adamo N, 1996. Summertime winds and direct cyclonic circulation: Observations from Lake Geneva. Ann. Geophys. 14:1207–1220.

Liardon J-L, Barry DA, 2017. Adaptable imaging package for remote vehicles. HardwareX 2:1–12.

Liss PS, 1983. Gas Transfer: Experiments and Geochemical Implications, p. 241–298 In: Liss PS and WGN Slinn (eds.), Air-Sea Exchange of Gases and Particles, Dordrecht: Springer Netherlands.

Liss PS, Duce RA, 1997. The Sea Surface and Global Change. Cambridge University Press, Cambridge, UK: 535 pp.

MacIntyre S, Amaral JHF, Melack JM, 2021a. Enhanced turbulence in the upper mixed layer under light winds and heating: implications for gas fluxes. J. Geophys. Res. Oceans 126:e2020JC017026.

MacIntyre S, Bastviken D, Arneborg L, Crowe AT, Karlsson J, Andersson A, Gålfalk M, Rutgersson A, Podgrajsek E, Melack JM, 2021b. Turbulence in a small boreal lake: Consequences for air–water gas exchange. Limnol. Oceanogr. 66:827–854.

Mahrt L, Hristov T, 2017. Is the influence of stability on the sea surface heat flux important? J. Phys. Oceanogr. 47:689–699.

Marmorino GO, Smith GB, 2006. Reduction of surface temperature in ocean slicks. Geophys. Res. Lett. 33:L14603.

Marmorino GO, Smith GB, Toporkov J V, Sletten MA, Perkovic D, Frasier SJ, 2008. Evolution of ocean slicks under a rising wind. J. Geophys. Res. Oceans. 113:C04030.

Marmorino GO, Toporkov JV, Smith GB, Sletten MA, Perkovic D, Frasier S, Judd KP, 2007. Ocean mixed-layer depth and current variation estimated from imagery of surfactant streaks. IEEE Geosci. Remote Sens. Lett. 4:364–367.

Masse AK, Murthy CR, 1990. Observations of the Niagara River thermal plume (Lake Ontario, North America). J. Geophys. Res. Oceans 95:16097–16109.

McKinney P, Holt B, Matsumoto K, 2012. Small eddies observed in Lake Superior using SAR and sea surface temperature imagery. J. Gt. Lakes Res. 38:786–797.

Meyers TP, Dale RF, 1983. Predicting daily insolation with hourly cloud height and coverage. J. Appl. Meteorol. Climatol. 22:537–545.

Minaudo C, Odermatt D, Bouffard D, Rahaghi AI, Lavanchy S, Wüest A, 2021. The Imprint of Primary Production on High-Frequency Profiles of Lake Optical Properties. Environ. Sci. Technol. 55:14234–14244.

Monin AS, Obukhov AM, 1954. Basic laws of turbulent mixing in the surface layer of the atmosphere. Tr Akad Nauk SSSR Geophiz Inst. 24:163-187. Adapted by Keith McNaughton (2008) from a translation by John Miller (1959).

Murphy KR, Stedmon CA, Waite TD, Ruiz GM, 2008. Distinguishing between terrestrial and autochthonous organic matter sources in marine environments using fluorescence spectroscopy. Mar. Chem. 108:40–58.

Olesen B, Maberly S, 2001. The effect of high levels of visible and ultra-violet radiation on the photosynthesis of phytoplankton from a freshwater lake. Arch. Hydrobiol. 151:301–315.

Pereira R, Ashton I, Sabbaghzadeh B, Shutler JD, Upstill-Goddard RC, 2018. Reduced air–sea CO2 exchange in the Atlantic Ocean due to biological surfactants. Nat. Geosci. 11:492–496.

Price JF, Weller RA, Pinkel R, 1986. Diurnal cycling: Observations and models of the upper ocean response to diurnal heating, cooling, and wind mixing. J. Geophys. Res. Oceans. 91(C7):8411–8427.

Qiao F, Yuan Y, Deng J, Dai D, Song Z, 2016. Wave–turbulence interaction-induced vertical mixing and its effects in ocean and climate models. Philos. Trans. R. Soc. Math. Phys. Eng. Sci. 374:20150201.

Rahaghi AI, Lemmin U, Barry DA, 2019a. Surface water temperature heterogeneity at subpixel satellite scales and its effect on the surface cooling estimates of a large lake: Airborne remote sensing results from Lake Geneva. J. Geophys. Res. Oceans 124:635–651.

Rahaghi AI, Lemmin U, Cimatoribus AA, Barry DA, 2019b. The importance of systematic spatial variability in the surface heat flux of a large lake: A multiannual analysis for Lake Geneva. Water Resour. Res. 55:10248–10267.

Rahaghi AI, Lemmin U, Cimatoribus AA, Bouffard D, Riffler M, Wunderle S, Barry DA, 2018. Improving surface heat flux estimation for a large lake through model optimization and two-point calibration: The case of Lake Geneva. Limnol. Oceanogr. Methods 16:576–593.

Rahaghi AI, Lemmin U, Sage D, Barry DA, 2019c. Achieving high-resolution thermal imagery in low-contrast lake surface waters by aerial remote sensing and image registration. Remote Sens. Environ. 221:773–783.

Razmi AM, Barry DA, Bouffard D, Vennemann T, Barry CE, Lemmin U, 2017. Currents of Lake Geneva, p. 141-172 In: Micropollutants in Large Lakes, Boca Raton and EPFL Press.

Romano JC, 1996. Sea-surface slick occurrence in the open sea (Mediterranean, Red Sea, Indian Ocean) in relation to wind speed. Deep Sea Res. Part Oceanogr. Res. Pap. 43:411–423.

Salter ME, 2010. A role for natural surfactants in air-sea gas exchange? (Doctoral dissertation). Newcastle upon Tyne, UK: University of Newcastle upon Tyne.

Savelyev IB, Buckley MP, Haus BK, 2020. The impact of non-breaking waves on wind-driven ocean surface turbulence. J. Geophys. Res. Oceans 125:e2019JC015573.

Schuler DL, Lee JS, 2006. Mapping ocean surface features using biogenic slick-fields and SAR polarimetric decomposition techniques. IEEE Proc. - Radar Sonar Navig. 153:260–270.

Shen H, Perrie W, Wu Y, 2019. Wind drag in oil spilled ocean surface and its impact on wind-driven circulation. Anthr. Coasts 2:244–260.

Smith SD, 1988. Coefficients for sea surface wind stress, heat flux, and wind profiles as a function of wind speed and temperature. J. Geophys. Res. Oceans 93:15467–15472.

Soulignac F, Lemmin U, Ziabari SMH, Wynn HK, Graf B, Barry DA, 2021. Rapid changes in river plume dynamics caused by advected wind-driven coastal upwelling as observed in Lake Geneva. Limnol. Oceanogr. 66:3116–3133.

Stedmon CA, Bro R, 2008. Characterizing dissolved organic matter fluorescence with parallel factor analysis: A tutorial. Limnol. Oceanogr. Methods 6:572–579.

Taylor PK, Yelland MJ, 2001. The dependence of sea surface roughness on the height and steepness of the waves. J. Phys. Oceanogr. 31:572–590.

Tejada-Martínez AE, Hafsi A, Akan C, Juha M, Veron F, 2020. Large-eddy simulation of small-scale Langmuir circulation and scalar transport. J. Fluid Mech. 885:A5.

Thompson EJ, Moum JN, Fairall CW, Rutledge SA, 2019. Wind limits on rain layers and diurnal warm layers. J. Geophys. Res. Oceans 124:897–924.

Tsai W, Liu K-K, 2003. An assessment of the effect of sea surface surfactant on global atmosphere-ocean CO_2 flux. J. Geophys. Res. Oceans. 108(C4):3127.

Tsai WT, 1996. Impact of a surfactant on a turbulent shear layer under the air-sea interface. J. Geophys. Res. Oceans 101:28557–28568.

Vanderplow B, Soloviev AV, Dean CW, Haus BK, Lukas R, Sami M, Ginis I, 2020. Potential effect of bio-surfactants on sea spray generation in tropical cyclone conditions. Sci. Rep. 10:19057.

Veron F, Melville WK, 2001. Experiments on the stability and transition of wind-driven water surfaces. J. Fluid Mech. 446:25–65.

Wang C, Fei J, Ding J, Hu R, Huang X, Cheng X, 2017. Development of a new significant wave height and dominant wave period parameterization scheme. Ocean Eng. 135:170–182.

Ward B, 2006. Near-surface ocean temperature. J. Geophys. Res. Oceans 111:C02004.

Watson AJ, Bock EJ, Jähne B, Asher WE, Frew NM, Hasse L, Korenowski GM, Merlivat L, Phillips LF, Schluessel P, Woolf DK, Liss PS, 1997. Report Group 1 – Physical processes in the microlayer and the air-sea exchange of trace gases, p. 1–34 In: Liss PS and RA Duce (eds.), The Sea Surface and Global Change, Cambridge: Cambridge University Press.

Whitney JL, Gove JM, McManus MA, Smith KA, Lecky J, Neubauer P, Phipps JE, Contreras EA, Kobayashi DR, Asner GP, 2021. Surface slicks are pelagic nurseries for diverse ocean fauna. Sci. Rep. 11:3197.

Wolfbeis OS, 1985. The fluorescence of organic natural products, p. 167–370 In: Schulman SG (ed.), Molecular Luminescence Spectroscopy. Part I: Methods and Applications, New York, NY: Wiley.

Woolway RI, Jones D, Feuchtmayr H, Maberly SC, 2015. A comparison of the diel variability in epilimnetic temperature for five lakes in the English Lake District. Inland Waters 5:139–154.

Wüest A, Bouffard D, Guillard J, Ibelings BW, Lavanchy S, Perga M-E, Pasche N, 2021. LéXPLORE: A floating laboratory on Lake Geneva offering unique lake research opportunities. WIREs Water 8:e1544.

Wurl O, Bird K, Cunliffe M, Landing WM, Miller U, Mustaffa NIH, Ribas-Ribas M, Witte C, Zappa CJ, 2018. Warming and inhibition of salinization at the ocean's surface by cyanobacteria. Geophys. Res. Lett. 45:4230–4237.

Wurl O, Stolle C, Van Thuoc C, The Thu P, Mari X, 2016. Biofilm-like properties of the sea surface and predicted effects on air-sea CO_2 exchange. Prog. Oceanogr. 144:15–24.

Yusup Y, Liu H, 2016. Effects of atmospheric surface layer stability on turbulent fluxes of heat and water vapor across the water–atmosphere interface. J. Hydrometeorol. 17:2835–2851.

Zappa CJ, Laxague NJM, Brumer SE, Anderson SP, 2019. The impact of wind gusts on the ocean thermal skin layer. Geophys. Res. Lett. 46:11301–11309.

Zeng X, Zhao M, Dickinson RE, 1998. Intercomparison of bulk aerodynamic algorithms for the computation of sea surface fluxes using TOGA COARE and TAO data. J. Clim. 11:2628–2644.

Žutić V, Ćosović B, Marčenko E, Bihari N, Kršinić F, 1981. Surfactant production by marine phytoplankton. Mar. Chem. 10:505–520.